

# Fabrication of New Generation of Nanocomposite Ceramic Coatings on Magnesium Alloys for Orthopedic Applications

Amin Kolooshani

IAU

Amin Kolahdooz

IAU

Amirsalar Khandan (✉ [amir\\_salar\\_khandan@yahoo.com](mailto:amir_salar_khandan@yahoo.com))

Amirkabir University of Technology

---

## Research Article

**Keywords:** Nanocomposite, Magnetite nanoparticles, Surface Engineering, Orthopedic Prosthesis, Electrophoretic deposition

**Posted Date:** November 12th, 2020

**DOI:** <https://doi.org/10.21203/rs.3.rs-103485/v1>

**License:**  This work is licensed under a Creative Commons Attribution 4.0 International License.

[Read Full License](#)

---

# Abstract

properties such as biocompatibility and proper bioactivity response. The aim of the present study was to investigate the bioactivity of wollastonite-hydroxyapatite (WS-HA) bio-nanocomposite for the treatment of orthopedic prosthesis coatings approaches by adding magnetic nanoparticles ( $\text{Fe}_3\text{O}_4$ ; MNPs) and single walled carbon nanotubes (SWCNTs) to the matrix. Bio-nanocomposite coated on AZ91 for 40 minutes at 40 volts using electrophoretic deposition (EPD) and after that the heat treatment performed at 550-650°C for 1 hour. The coats were incubated in simulated body fluid (SBF) and phosphate buffer saline (PBS) for 28 days to detect and confirm apatite-like layer formation. X-ray diffraction (XRD), atomic force microscope (AFM) and scanning electron microscopy (SEM) techniques were used to characterize the phase and morphology of the coated sample. Inductively coupled plasma optical emission spectroscopy (ICP-AES) tests were used to evaluate the concentrations of calcium and silicon ions. The finding from the present study showed the successful coating with 10 wt% MNPs added to the WS bio-nanocomposite with proper biological and chemical properties. Bio-nanocomposite coating can be considered as a suitable candidate for orthopedic coating applications due to its favorable bioactivity.

## Introduction

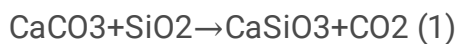
One of the most important bioceramics which have been used in regenerative medicine particularly orthopedic application is new calcium silicates (CSs), wollastonite ( $\text{CaSiO}_3$ ) nanoparticle enhancing bone formation of the implanted prosthesis [1]. These bioactive ceramics can enhance new bone tissue formation by creating a tight bond between implant and the host bone after implantation [2]. CSs and calcium phosphates (CaPs) are chemically similar to the inorganic structure of the human bone tissue [3]. The reason that available implants are often eventually rejected is due to the large grain size and the surfaces contaminations and impurities in the superficial part of the prosthesis [4-5]. The use of ceramic-metal and ceramic-polymer coatings is increasing owing to the proper bone response, faster stability and fixation [6-8] around the tissue of a metal implant such as titanium, stainless steel or magnesium alloys [9-10]. The most widespread use of hydroxyapatite (HA) coatings for dental implants are metallic root and used for orthopedic fracture and knee replacement [11-12]. It has been proposed that dimensional stability against thermal changes makes precision machining of Mg alloys easier, as well as high fluidity used in casting that lead to creation of suitable orthopedic prosthesis [13-16]. Researchers showed that using stainless steel 316 L coatings increased the corrosion resistance of the substrate [17]. Besides, by applying hydroxyapatite-titanium composite coating on stainless steel, an improvement through the corrosion resistance of stainless steel will occur. On the other hands, Tiwari et al. [19] applied silica-alumina coatings on stainless steel by sol-gel method and increased the corrosion resistance of the substrate. Fathi et al. [20] achieved good adhesion without cracking and uniformity by applying sol-gel bioactive glass coatings on stainless steel. this method also increased the biocompatibility and corrosion resistance for the substrate. Salehi et al. [21] applied hydroxyapatite-zirconia nanocomposite coatings on stainless steel with minimal flawed coating; however little effect on substrate corrosion resistance and preventing electrochemical reactions at the substrate surface occurred. Fu et al. [22] applied titanium

oxide coatings on stainless steel by plasma nitride method with low crack coating and good strength which obtained by proper heat treatment and improved corrosion resistance. Mechanical activation (MA) is a type of materials preparation process in which the powder mixture is affected by high-energy collisions between the mill components (pellets and chambers). This process is often carried out in a neutral atmosphere. The mechanical activation process is used to produce alloys and intermetallic compounds and amorphous materials. One of the most interesting applications of the MA method is its ability to produce nanocrystalline structures. In the current study, two types of ceramic coat were conducted using electrophoretic deposition (EPD) technique on magnesium alloy. The mechanical and chemical properties of the wollastonite-single walled carbon nanotube and wollastonite-magnetite nanoparticles were coated on AZ91 with EPD technique. The aim of the present study was to investigate the bioactivity of wollastonite-hydroxyapatite (WS-HA) bio-nanocomposite for the treatment of orthopedic prosthesis coatings approaches by adding magnetic nanoparticles ( $\text{Fe}_3\text{O}_4$ ; MNPs) and single walled carbon nanotubes (SWCNTs) to the based matrix.

## Materials And Methods

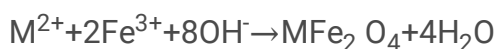
### Wollastonite powder preparation

The amount of raw materials required for the fabrication of 10 g wollastonite powder with talc (50-100 nm, 99% purity, Merck, Germany), calcite (99% purity, Merck, Germany) and silica (50-100 nm, 99% purity, Sigma-Aldrich, USA) were 4.47 wt%, 3.67 wt%, and 1.5 wt%, respectively. The following materials were mechanically activated 10 hours and the mixture was heated to 1200°C for 3 hours. To analyze the phase structure and confirm its complete synthesise process, X-ray diffraction (XRD) technique was used.



### Magnetite nanoparticle preparation

The methods of synthesis of magnetic nanoparticles (MNPs) in the liquid phase can be mentioned as co-precipitation. The co-precipitation is the simplest and most efficient chemical technique for fabrication of ferrites nanoparticle [24]. Usually, the synthesis of iron oxide nanoparticles ( $\text{Fe}_3\text{O}_4$ ,  $\gamma\text{-Fe}_2\text{O}_3$ ) and ferrites in the aqueous medium is accomplished by the co-precipitation method via the following 2 reaction:



$\text{M}^{2+}$  can be different elements such as  $\text{Fe}^{2+}$ ,  $\text{Mn}^{2+}$ ,  $\text{Co}^{2+}$ ,  $\text{Cu}^{2+}$ ,  $\text{Mg}^{2+}$ ,  $\text{Zn}^{2+}$ ,  $\text{Ni}^{2+}$ .

### Ceramic suspension preparation

Ethanol (99% purity, Merck, Germany) is used as the suspension solvent in the EPD coating process. Deionized distilled water is used in the process as a detergent (Prepared at Scientific Research Town,

Isfahan University of Technology). In the present study, triethanolamine (Merck-Germany) was used as dispersant. Sartorius Digital Balance with 0.0001-gram accuracy was used to weigh the consumables. Stirring technique was used to prepare and homogenize the suspension solution. The EPD can charged powder particles that are dispersed or suspended in a liquid medium (isopropanol-ethanol). Then, the solution is adsorbed and deposited on an oppositely charged conductive substrate (Ti) with DC electric field by applying voltage of 30 to 50 volts. Isopropanol was used as a solvent to produce the hydroxyapatite/wollastonite (HA/WS) suspension. The solution was prepared 100 cc of the solvent was poured into the human and then stirred with hydroxyapatite, wollastonite with constant weight percentages, and magnetic additives and single walled carbon nanotubes. The solution was then stirred for 40 minutes until the powders were well dispersed in the solvent. Then, 1.6 g of triethanolamine (TEA) was added to the desired suspension. as final step, the container containing the desired materials was placed on the stirrer at room temperature for 48 hours to allow the suspension to disperse well. The suspension was then sonicated in the stirrer for 200 minutes. In this study, wollastonite nanocrystalline powder was first prepared by mechanical grinding at 1200°C, followed by a constant weight ratio (10 wt.%) of MNPs and SWCNT by nanocomposite blend molding and mixing. The wollastonite powder was synthesized using mechanical activation (MA) and thermal synthesis methods. The bio-nanocomposite powders were then coated on the substrate for 5 minutes using electrophoretic process (EPD) at voltages of 30, 40 and 50 V as shown in the schematic diagram. After the EPD process, heat treatment is performed for 1 hour at a temperature of 550-650°C for the sintering of bio-nanocomposite particles. X-ray diffraction (XRD) and scanning electron microscopy (SEM) techniques are used to characterize the phase and morphology of the coating. Biological evaluation (bioactivity) of bio-nanocomposite coatings immersed in simulated body fluid (SBF) for 28 days was performed. The SEM image was used to detect and confirm bone-like layer which formed on the surface of porous coats. The microstructure and roughness of the specimens are also examined according to ASTM standard. In addition, the micron size layer of coat on magnesium alloy is simulated mechanically as a porous composite by ABAQUS software version 16. Hydroxyapatite-magnetite and hydroxyapatite-single walled carbon nanotube composite coatings were made by constant weight percentages (10 wt%) EPD (Figure 1). Figure 2 shows the EPD technique set up for coating of ceramic solution on Mg alloy. The biological response of the coat such as weight loss and degradation rate were evaluated in the SBF and PBS for 28 days. The biggest limitation of *in vitro* tests is that systemic response cannot be assessed, nor can the association between the information gathered from *in vitro* tests and the medical function of the prosthesis in the real sample for the human body be established [17-25]. The phenomenon of temperature rise is related to the increase of hydroxyapatite crystals as well as decrease in size of HA with increasing temperature. Based on the XRD spectra presented, it can be seen that bone ash begins to crystallize at 600°C without being decomposed or transformed into other calcium phosphate family structures like tricalcium phosphate, beta and tetra calcium phosphate ( $\alpha$ -TCP) are not observed in any of the temperatures below 900°C. The sharp, narrow, and sharp peaks are completely related to hydroxyapatite and indicated the high purity and crystallinity of the material produced at this temperature. According to the observations, it is clarified that the resulting product is single-phase hydroxyapatite and no additional stable phase was seen. There was also a good fit between the product diffraction peaks with JCPDS: 09-432 (this standard applies to X pert

software, pert XRD device). The primary XRD peaks of the hydroxyapatite powder at 900°C indicate the formation of the HA powder, which is used for medical applications because of its similarity to bone apatite. Importantly, the difference in the diffraction pattern indicates the difference in the average crystalline grain size [26-33]. These results confirm the presence of the HA phase in the XRF test for HA and high purity and the amount and type of impurities in the carbon powder. This analysis revealed that calcium and phosphorus are the main constituents of the hydroxyapatite powder and that sodium and magnesium are impurities in it. It also showed that the HA powder produced was 96% pure and its mineral impurities included Na<sub>2</sub>O (1 wt%) and MgO (1 wt%). Calcium to phosphorus ratio (Ca/P) was calculated with the ratio of 1.90. The sintering of the coats performed at 650-550°C temperatures for 1 hour as represented in literature survey.

## Materials characterization

### XRD analysis

Phase characterization of bio-nanocomposite powders was performed using X-ray diffraction (XRD) (XRD, Philips X Pert-MPD System). The XRD pattern was obtained using Cu-K $\alpha$  lamp with wavelength  $\lambda = 1/5406^\circ\text{A}$  in the range  $0 < 2\theta < 90^\circ$ , step 0.02 and time for each step 1 second. Then, the XRD pattern was performed by comparing the angle and intensity of the diffraction peaks with the information in the standard cards. The XRD analysis was used as a powerful non-destructive technique for characterization of the coats to determine the phase transition and crystalline orientations with obtaining an average grain size with the crystallinity before and after sintering process. The modified Scherrer equation (MSE) was used to measure the crystal size of the wollastonite nanoparticles and its grain size determination. For this purpose, three peaks of each phase were selected in XRD pattern and the width of the higher peak was calculated.

$$B \cos\theta = \frac{0.89\lambda}{L} \quad (3)$$

Where L is the grain size (nm),  $\lambda$  the wavelength (for the copper tube equals 0.1542 nm), the K-shaped factor (0.89), B the width peak selected at half height in radians, and  $\theta^\circ$  is the peak angle. In this approach, by drawing Ln B diagrams in terms of Ln (1/Cos  $\Theta$ ) and obtaining the width of the source which is actually Ln (K $\lambda$ /L), one can obtain the average value of the crystal size L. The values of K,  $\lambda$  are 1.54 and 0.89, respectively.

### SEM analysis

The microstructure, particle distribution and morphology of composite powders were investigated using scanning electron microscopy (SEM) using LEO tools. First the samples were coated with a very thin layer of gold to increase the electrical conductivity of the specimen surface and to enhance the clarity of the

images. Also, the cross-sections of the coated sample were examined to detect the surface pores using Image-J software.

### XRF analysis

The HA nanoparticle was analyzed using elemental analysis using X-ray fluorescence spectroscopy (XRF; Bruker-S4 Pioneer, Germany)

### ICP-OES analysis

Inductively coupled plasma-optical emission spectroscopy (ICP-OES) was used to measure calcium ion after immersion in the SBF solution. The surface roughness of the samples was measured using roughness device at Islamic Azad University. It is important to notice that due to different roughness calculation algorithms, affective parameters, accurate information cannot be obtained using this technique. Therefore, the roughness qualitative measurement method was used by the roughness tester with three variables Ra, Rz and Rmax. The chemical composition of the simulated body fluid (SBF) similar to human blood plasma is compared in Table 1 in which developed by Kokubo procedure [26].

### Biological testing

The biological behavior of the specimen in SBF was investigated to control and monitor the release and degradation rate of surface coats after 28 days at 37°C. A volume of SBF was added and kept in the incubator for 1, 3, 7, 14, 21, and 28 days at  $37 \pm 0.1^\circ\text{C}$ . The coatings were first rinsed with distilled water and then dried at ambient temperature for 24 hours. The surface of the coatings was examined by SEM micrograph and spectroscopic to determine the amount and morphology of the biological apatite deposited on its surface during immersion. Also, an ionomeric test was conducted to measure the amount of calcium, phosphorus and magnesium ions in solution to compare the changes of these ions on days considered by ICP-OES (Perkin DV7300-Elmer, size).

### Wetting evaluation

The samples surface wettability was monitored using liquid contact angle with different equations and drop let technique with using an electron microscope and CCD camera imaging after 30 seconds. The wettability analysis utilizes forces when immersing a liquid to obtain surface tension on the surface of HA-WS-MNPs coated on Mg-AZ91 with EPD technique.

### Biodegradability Test (PBS)

The biodegradability of the coated AZ91 coatings soaked in PBS was evaluated with acidity of 7.4 for 21 days. The dissolution of the coated specimen was measured in the 100 mL of PBS with the sample size of 1×1 cm piece stored in a CO<sub>2</sub> incubator at 37°C after being placed in a falcon containing. The samples were removed from the PBS solution on days 1, 3, 7, 14, and 21 dried at 37°C for 2 hours. Weight loss and destruction rates of the coated samples were calculated by the equation 4.

$$\text{Degradation}(\%) = \left( \frac{W_i - W_f}{W_i} \right) \times 100 \quad (4)$$

$W_i$  is the initial dry weight of the sample and  $W_f$  is the dry weight of the sample after degradation in PBS.

## Results

The XRD pattern shows pure bioceramic powders, magnetic powders composite, and single walled carbon nanotubes (Figure 3a-d). By adding WS the toughening mechanism of the composites have enhanced, this procedure changed the crystallization temperature of the composite to a significant range, and subsequently the crystallization altered the fracture mechanism of the prosthesis. Based in the XRD, the crystallite size of the powders was 40-100 nm. The HA and WS nanoparticles showed an average particle size of less than 100 nm. The nanoparticles had a spherical and crystal structure, which indicates high purity of the powders. Minor impurities were detected in the range of 60 to 80 that was owing to the composition and milling time. The XRD pattern of the HA at angles  $2\theta$  equal to  $23.2^\circ$ ,  $26^\circ$ ,  $29.3^\circ$ ,  $32.2^\circ$ ,  $46.6^\circ$  and  $49.4^\circ$  was seen with its corresponding peaks. The sample contains a series of peaks from about 30 degrees to  $70^\circ$  (figure 3b). These sharp peaks in the composite specimen confirm the presence of a magnetic nanocrystalline network throughout the nanocomposite. These changes in the composite reflect the change in the crystalline structure of the base material, because the magnetic nanoparticles are completely amorphous regarding to the XRD pattern. There are various methods for the synthesis of MNPs, such as microemulsion, gamma irradiation, microwave irradiation, hydrothermal and sol-gel methods. These methods can be used to prepare and control the size and morphology of magnetite nanoparticles by adjusting the growth parameters. The HA powder on the coating is on different alloys and the functional group microstructures are not desired. The XRD pattern of the carbon nanotube powder showed that crystallite size of which was 10-20 nm. It is important to notice that the amorphous microstructure strengthens the mechanical properties of the coated prosthesis including elastic modulus and fracture toughness value. The particle size distribution of HA, WS, SWCNT, MNPs and HA powders with single walled carbon nanotubes and HA powders with 10 wt% magnetic nanoparticles have the average size 10-800 nm (Figure 3 and 4). The effect of WS nanopowder addition to HA showed a chemical enhancement as well as agglomeration phenomenon. The composite proved to be effective because of the  $\text{SiO}_2$  present in the WS nanopowder that can contain large amounts of  $\text{Fe}_3\text{O}_4$  nanoparticles. In the XRD spectrum, the highest peak corresponds to HA at  $31.5^\circ$ , with compounds similar to wollastonite, and at shorter peaks phases such as HA are observed. The crystallite size of this homogenized powder was 50 nm. In the XRD spectrum of composite samples containing 10 wt% by weight of magnetic particles and carbon nanotubes, the highest peak corresponds to the HA phase. So, by the increasing the bioceramics and magnetic nanoparticles, the composite peaks have decreased particularly at 10 and the peaks of the magnetic nanoparticles have been sharpened at  $30^\circ$  to  $35^\circ$ . One of the most important factors of reaction temperature is the concentration of iron salts solution and the concentration of precipitating material in the process of material synthesis. The impact of these factors

has been examined in various studies [44-48]. SEM analyses of HA and wollastonite bioceramic powders revealed that composite powders acted as enhancer to improve their chemical properties (figure 6 and 7). Besides, the ceramic nanoparticles were nano and micron sized and had a flame-retardant structure. They were branches of the species that were clearly shown together with spherical hydroxyapatite nanoparticles. Microscopic images showed the differentiation between spherical HA nanoparticles with porous dendritic horned nanoparticles. In bone tissue engineering, the porosity and compressive strength of coatings should be balanced. The composite ceramic coatings were fabricated by electrophoretic method. The final product is a coating with a medium porosity of about 40-60 microns. On the other hands, comparison of the microstructure of the ceramic coating with 10 wt% magnetite and 10wt% single walled carbon nanotube, showed that by adding 10 wt% MNPs does not make difference in the structural shape of the porous coating and the porosity. The hardness of the samples increased with the addition of SWCNT, whereas the hardness decreased with the change of the substrate from magnesium to titanium. The numbers reported by the Vickers hardness test showed that the coating on the titanium alloy was compatible with the magnetic composite coating. The elastic modulus was affected by the substrate and the reinforcement modifies the elastic modulus, consequently, by adding SWCNT (Figure 9). The AFM microscope image in Figure 10 shows that in the sample with Mg substrate, the coating has a thickness of about 2-5 microns, and the surface of the coating at 10-micron intervals has intermittent wavelength and porosity. the average surface roughness of the sample is observed to be about 10-20 microns. (figure 10-11). It is very low but with very low porosity and some extruded nanoparticles show agglomeration of the coating surface and its surface under the magnesium layer due to free electrons has less adhesion than titanium. The AFM microscope image of the sample with Mg substrate, the coating has a thickness about 2-5 microns. The graphs show that the surface of the coating have 10-micron intervals wavelength. The average surface roughness of the sample measured about 10-20 microns. The AFM microscope image shows the surface of bio-nanocomposite coated on magnesium substrate with 8  $\mu\text{m}$  intervals and roughness. The obtained result from the coated surface indicated that some extruded nanoparticles with agglomerate shape.

Fabrication and deposition of composite coating on magnesium can prepare a required biological, mechanical properties and surface adhesion for the samples. The suitable coats can provide a suitable environment for oxygen exchange as well as adequate bone growth for implants due to the pores in its microstructure. However, the solubility of the porous coats in the solution due to its permeability change the pH concentration to higher level after 3 days. most of the changes occurred in the first three days, so that after 7 days the pH reached to 7.7. The evidence for such changes can be due to the separation of Si-O-Si bonds from WS in the composite surface. The ICP-OES and pH changes indicated that the calcium and iron ions attracted to each other regarding their high electronegativity from the surface of the coating after immersion in the SBF solution. These heavy ions displacements are important in bone formation process. The observation indicated that all the changes and calcium ions release in the solution leads the absorption of  $\text{H}^+$  ions.

The apatite layer formation or the formation of silanol groups on the AZ91 surface leads to a negative charge on the porous microstructure surface. The calcium ions positively charged to the coated surface, resulted in a decrease in the pH value in the solution followed by a positive charge on the surface, with negatively charged phosphate groups on the surface that caused calcium-phosphate groups precipitation. This is the first time that a new generation of calcium silicates ceramic has been synthesized to produce porous coatings with favorable mechanical properties, antibacterial response, utilized in affordable and affordable natural bioceramics.

th results from the present study showed that the coating and substrate material affect the hardness of the coatings. The concentration or pH changes of all solutions were measured on the first day which shows similar value to human blood plasma. After 21 days, the solubility of the porous coating's changes because of their soluble permeability and pH changes. Most of the changes occurred in the first days, so that after 7 days the pH reached from 7.4 to 7.7, which can be introduced to be due to the breakage of Si-O-Si bonds from wollastonite. Calcium and iron ions degraded from the surface of the coating into the ringier solution after first week. This ion displacement, which actually releases calcium and iron ions from the coating surface to the saline and attracted into the solution. The absorption of  $H^+$  and breaks the chemical bonds, resulting in the formation of silanol groups on the porous coated surface that resulted in negative charge on the coated surface. The positive charged calcium ions are adsorbed to the coated surface, resulted in a decrease of pH value in the solution. Also, with negative charged by phosphate groups on the surface leads proper calcium-phosphate groups to be formed. Several researchers focus on synthesize of magnetite nanoparticles using various technique. Citrate coated magnetite nanoparticles (NPs) were prepared by a modified coprecipitation technique in the presence of sodium citrate and sodium acetate [40-45].

## Conclusions

The most important results of this study are:

1. Wollastonite nanopowder was prepared by mechanical alloying by calcining at 1200°C.
2. Homogeneous composite was prepared by single-phase mechanical activation (MA) method.
3. Porous coating was made on three alloys with magnetic and single walled carbon nanotube composites containing 10% by weight of magnetite and carbon nanotube by electrophoretic method.
4. The structure of the hydroxyapatite-MNPs nanocomposite coating was prepared at 550°C and the pores were 45-34% spherical and 45-34% true porosity.
5. The strength and tensile strength of the coatings were affected by the addition of carbon nanotube and magnetic nanoparticles.
6. The results of biodegradation and bioactivity studies showed that the bio-nanocomposite coatings contain bioactive magnetic nanoparticles.
7. Examination of changes in the concentration of ions released from magnetic coatings in physiological solution showed that by adding 10 wt% to the magnetism substrate, the dissolution

rate of bio-nanocomposite coatings decreased.

8. Magnetite and hydroxyapatite grain sizes in these coatings were obtained in the range of 40 to 60 nm, respectively.
9. SEM images showed relatively good adhesion between the substrate and the coating.
10. Formation of hydroxyapatite carbonate layer was observed on samples with magnetically immersed in body simulation solution.
11. Further release of silicon ions (from wollastonite nanoparticles) accelerated the formation of the apatite layer on the surface of the material in the simulated body solution.
12. The coatings placed in the furnace at 550°C have better adhesion to lower temperatures and the growth of micro-cracks was less pronounced in all samples.
13. Formation of apatite (formation apatite) in the sample of 10 wt% MNPs is the highest.
14. Bioactive wollastonite can be produced by HA by mechanical activation method and has good adhesion to titanium substrate. This can be a good option for orthopedic coatings.

## **Abbreviations**

Not applicable.

## **Declarations**

### **Ethics approval and consent to participate**

Not applicable.

### **Consent for publication**

All authors read and approved the final manuscript and consented to publication.

### **Availability of data and materials**

No data were used from internet data sources.

### **Competing Interests**

The authors report no conflicts of interest in this work.

### **Funding**

This work was not supported or grants from the any Science Foundation. The work is self-funded and the funders had role in study design, data collection and analysis, decision to publish, or preparation of the manuscript.

### **Authors' contributions**

All the researcher participated in the design of this study. Khandan performed the statistical analysis. Samandari collected important background information. Khandan drafted the manuscript. All authors read and approved the final manuscript.

## ACKNOWLEDGEMENTS

The authors would like to extend their gratitude for the support provided by the New Technology Research Centre, Tehran, and Iran.

## CONFLICT OF INTEREST

The authors confirm that this article

## References

- [1] Musfirah, A. H., & Jaharah, A. G. (2012). Magnesium and aluminum alloys in automotive industry. *Journal of Applied Sciences Research*, 8(10), 4865- 4875.
- [2] Farrokhi- Rad, M. (2018). Electrophoretic deposition of fiber hydroxyapatite / Titania nanocomposite coatings ceramic International, 44(1). 622-630.
- [3] Chen, X., Chen, S., Liang, L., Hong, H., Zhang, Z., & Shen, B. (2018). Electrochemical behavior of EPD synthesized graphene coating on titanium alloys for orthopedic implant application. *Procedia CIRP*, 71, 322-328.
- [4] Pansini, M., Dell' Agli, G., Marocco, A., Netti, P. A., Battista, E., Lettera, V., ... & Barrera, G. (2017).
- [5] Farrokhi- Rad, M., Shahrabi, T., Mahmoodi, S., & Khanmohammadi, S. (2017). Electrophoretic deposition of hydroxyapatite- chitosan- CNTs nanocomposite coatings. *Ceramics International*, 43 (5), 4663- 4669.
- [6] Bakhsheshi- Rad, H. R., Hamzah, E., Dias, G. J., Saud, S. N., Yaghoubidoust, F., & Hadisi, Z. (2017). Fabrication and characterization of novel ZnO/ MWCNT duplex coating deposited on Mg alloy by PVD coupled with dip-coating techniques. *Journal of Alloys and compounds*, 728, 159-168.
- [7] Khandan, A., Abdellahi, M., Ozada, N., & Ghayour, H. (2016). Study of the bioactivity, wettability and hardness behaviour of the bovine hydroxyapatite-diopside bio-nanocomposite coating. *Journal of the Taiwan Institute of Chemical Engineers*, 60, 538-546.
- [8] Ducheyne, P., Radin., Heughebaert, M., & Heughebaert, J.C. (1990). Calcium phosphate ceramic coatings on porous titanium: effect of structure and composition on electrophoretic deposition, vacuum sintering and in vitro dissolution. *Biomaterials*, 11 (4), 244- 254.

- [9] Murugan, N., Murugan, C., & Sundramoorthy, A. K. (2018). In vitro and in vitro characterization of mineralized hydroxyapatite / polycaprolactone- graphene oxide based bioactive multifunctional coating on Ti alloy for bone implant applications. *Arabian Journal of Chemistry*.
- [10] Ismail, R. A., Hamoudi, W. K., & Abbas, H. F. (2018). Electrophoretic deposition of hydroxyapatite-shrimp crusts nanocomposite thin films for bone implant studies. *IET Nanobiotechnology*.
- [11] Kus'nierczyk, K., & Basista, M. (2017). Recent advances phosphate composites as biodegradable implant materials. *Journal of biomaterials applications*, 31 (6), 878- 900.
- [12] Al-Rashidy, Z. M., Farag, M. M., Ghany, N. A., Ibrahim, A. M., & Abdel- Fattah, W. I. (2017). Aqueous electrophoretic deposition and corrosion protection of borate glass coatings on 316 L stainless steel for hard tissue fixation. *Surfaces and Interfaces*, 7, 125-133.
- [13] Nakajama, S. (1990). Experimental studies of healing process on reinforcement ceramic implantation in rabbit mandible. *Shika gakuho. Dental Science reports*, 90 (4), 525- 553.
- [14] Nakajima, S., Kurihara, Y., Wakatsuki, Y., & Noma, H. (1989). Physico-chemical characteristics of new reinforcement ceramic implant, *Shika gakuho. Dental Science reports*, 89 (11), 1709 – 1717.
- [15] Wu C.T., & Chang J. (2004). Synthesis and apatite-formation ability of akermanite. *Materials Letters*, 58 (19), 2415-2417.
- [16] Fathi, M.H., Doost Mohammadi, A., "Preparation and Characterization of Sol-gel bioactive Engineering", *Materials scienceA*, Vol. 474, pp. 128-133, 2008.
- [17] Głuzek, J., Masalski, J., Furman, P., & Nitsch, K. (1997). Structural and electrochemical examinations of PACVD TiO<sub>2</sub> films in Ringer solution. *Biomaterials*, 18(11), 789-794
- [18] Fathi, M. H., Mortazavi, V., & Moosavi, S. B. (2002). Designing, preparing and evaluation of novel HA/Ti composite coating for endodontic dental implant. *Journal of Dental Medicine*, 15(3), 39-54.
- [19] Tiwari, S. K., Mishra, T., Gunjan, M. K., Bhattacharyya, A. S., Singh, T. B., & Singh, R. (2007). Development and characterization of sol-gel silica-alumina composite coatings on AISI 316L for implant applications. *Surface and Coatings Technology*, 201(16-17), 7582-7588.
- [20] Fathi, M. H., & Doostmohammadi, A. (2009). Bioactive glass nanopowder and bioglass coating for biocompatibility improvement of metallic implant. *Journal of materials processing technology*, 209(3), 1385-1391.
- [21] Salehi, S., & Fathi, M. H. (2010, November). Preparation of sol-gel derived hydroxyapatite/yttria stabilized zirconia nanocomposite coatings on 316 L stainless steel. In 2010 17th Iranian Conference of Biomedical Engineering (ICBME) (pp. 1-4). IEEE.

- [22] Fu, T., Wen, C. S., Lu, J., Zhou, Y. M., Ma, S. G., Dong, B. H., & Liu, B. G. (2012). Sol-gel derived TiO<sub>2</sub> coating on plasma nitrided 316L stainless steel. *Vacuum*, 86(9), 1402-1407.
- [23] Tiwari, S.K., Mishra, T., Gunjan, M.K., Bahattacharyya, A., Singh, R., "Development and characterization of sol-gel silica-alumina composite coatings on AISI 316L for implant applications", *Surface & Coatings Technology*, Vol. 201, pp. 7582-7588, 2007.
- [24] Khandan, A., Abdellahi, M., Barenji, R. V., Ozada, N., & Karamian, E. (2015). Introducing natural hydroxyapatite-diopside (NHA-Di) nano-bioceramic coating. *Ceramics International*, 41(9), 12355-12363.
- [25] Eshtiagh. Hossein, H., Housaindokht, M., Chahkandi, M., "Effects of parameters of sol-gel process on the phase evolution of sol-gel-derived hydroxyapatite", *Materials Chemistry and Physics*, Vol. 106, pp.310-316, 2007.
- [26] Kokubo, T., Kim, H.M., Kawashita, M., "Novel bioactive materials with different mechanical properties", *Biomaterials*, Vol. 24, pp. 2161-2175, 2003.
- [27] Grandfield, K., Zhitomirsky, I., "GrandfieldElectrophoretic deposition of compositehydroxyapatite-silica-chitosan coatings", *Materials characterization*, Vol. 59, pp. 61-67, 2008.
- [28] Lu, X., Wang, Y.B., Liu, Y.R., Wang, J.X., Qu, S., Feng, B., Weng, J., "Preparation of HA/chitosan composite coatings on alkali treated titanium surfaces through sol-gel techniques", *Materials Letters*, Vol.61 , pp. 3970-3973, 2007.
- [29] Luciani, G., Costantini, A., Silvestri, B., Tescione, F., Brand, F., Pezella, A., "Synthesis, Structure and Bioactivity of pHEMA/SiO<sub>2</sub> hybrids derived in situ sol-gel Process", *Journal sol-gel Science Technology*, Vol.46, pp.166-175, 2008.
- [30] Evans, S.L., Gregson, P.J., "composite Technology in Load Bearing Orthopaedic Implants", *Biomaterials*, Vol.19, pp.1329-1342, 1998.
- [31] Lo'pez, D.A., Dura'n, A., Cere, S.M., "Electrochemical characterization of AISI 316L stainless steel in contact with simulated body fluid under infection conditions", *J Mater Sci: Mater Med*, Vol. 19, pp: 2137-2144, 2008.
- [32] Farker, D., Anna, C., *Corrosion of Metalitic implants and prosthetic devices*, *Corrosion metal Handbook*, ASM, Vol. 13, 1992.
- [33] Shara, D., "The Problem of corrosion in Orthopaedic Implant Mateials", *Orthopaedic Update (India)* 2, Vol. 9, No. 1, April 1999.
- [34] Janas, J., "Overview of Biomaterials and Their Use in Medical Devices", *Handbook of Materials for Medical Devices*, Chapter1, pp. 3-5, 2003.

- [35] Saha, P., Gally, E., "Corrosion of Titanium, Stainless steel, Chromium Cobalt Alloys, Amalgam-Orthopaedic & Dental Applications", *Metallic Biomaterials*, Vol. 74, pp.234-236, 2002.
- [36] Breme, J., Beihl, V., *Metallic Biomaterials, Handbook of Biomaterials properties*, Vol.23, pp. 135-143, 1998.
- [37] Shieu F.S., Deng M.J., Lin S.H., "Microstructure and a corrosion of a Type 316L Stainless steel", *Corrosion Science*, Vol.40, No.8, pp.1267-1279, 1998.
- [38] Fathi, M.H., Salehi, Saatchi,M., Mortazavi,A., Moosavi,V., "In vitro corrosion behavior of bio-ceramic, metallic and bio-ceramic metallic coated stainless steel dental implants", *Dental Materials*, Vol. 19, pp. 188-198, 2003.
- [39] Yashimista O., Emiko G., "comparison of Metal Release from Various Metallic Biomaterials in Vitro", *Biomaterials*, Vol. 26, pp.11-21, 2005.
- [40] RuizMoreno, R. G., Martinez, A. I., Castro-Rodriguez, R., & Bartolo, P. (2013). Synthesis and characterization of citrate coated magnetite nanoparticles. *Journal of superconductivity and novel magnetism*, 26(3), 709-712.
- [41] Kazemzadeh, H., Ataie, A., & Rashchi, F. (2012). In situ synthesis of silica-coated magnetite nanoparticles by reverse coprecipitation method. *Journal of superconductivity and novel magnetism*, 25(8), 2803-2808.
- [42] Sarma, L., Borah, J. P., Srinivasan, A., & Sarma, S. (2019). Synthesis and Characterization of Tea Polyphenol–Coated Magnetite Nanoparticles for Hyperthermia Application. *Journal of Superconductivity and Novel Magnetism*, 1-8.
- [43] Perez-Gonzalez, T., Rodriguez-Navarro, A., & Jimenez-Lopez, C. (2011). Inorganic magnetite precipitation at 25 C: a low-cost inorganic coprecipitation method. *Journal of superconductivity and novel magnetism*, 24(1-2), 549-557.
- [44] Yadav, B. S., Singh, R., Vishwakarma, A. K., & Kumar, N. (2020). Facile Synthesis of Substantially Magnetic Hollow Nanospheres of Maghemite ( $\gamma\text{-Fe}_2\text{O}_3$ ) Originated from Magnetite ( $\text{Fe}_3\text{O}_4$ ) via Solvothermal Method. *Journal of Superconductivity and Novel Magnetism*, 1-10.
- [45] Alaei, M., Atapour, M., & Labbaf, S. (2020). Electrophoretic deposition of chitosan-bioactive glass nanocomposite coatings on AZ91 Mg alloy for biomedical applications. *Progress in Organic Coatings*, 147, 105803.
- [46] Ren, Y., Babaie, E., & Bhaduri, S. B. (2018). Nanostructured amorphous magnesium phosphate/poly (lactic acid) composite coating for enhanced corrosion resistance and bioactivity of biodegradable AZ31 magnesium alloy. *Progress in Organic Coatings*, 118, 1-8.

[47] Kiran, A. S. K., Kumar, T. S., Perumal, G., Sanghavi, R., Doble, M., & Ramakrishna, S. (2018). Dual nanofibrous bioactive coating and antimicrobial surface treatment for infection resistant titanium implants. *Progress in Organic Coatings*, 121, 112-119.

[48] Akay, S. K., Peksoz, A., & Kara, A. (2018). Magnetic Responses of Divinylbenzene-Fe<sub>3</sub>O<sub>4</sub> Composite Film Deposited by Free Radical Polymerization Method. *Journal of Superconductivity and Novel Magnetism*, 31(3), 849-854.

## Tables

Table 1: Elemental analysis or X-ray Fluorescence spectroscopy of HAnanoparticles

Chemical element	Concentration (%w/w)
CaO	55.2
P <sub>2</sub> O <sub>5</sub>	37.5
Na <sub>2</sub> O	1.7
SO <sub>3</sub>	1.6
MgO	1.4
SiO <sub>2</sub>	1.2
Cl	0.89
H <sub>2</sub> O	0.83
Al <sub>2</sub> O <sub>3</sub>	0.65
SrO	0.60
K <sub>2</sub> O	0.55
C	0.42
CuO	0.40

## Figures

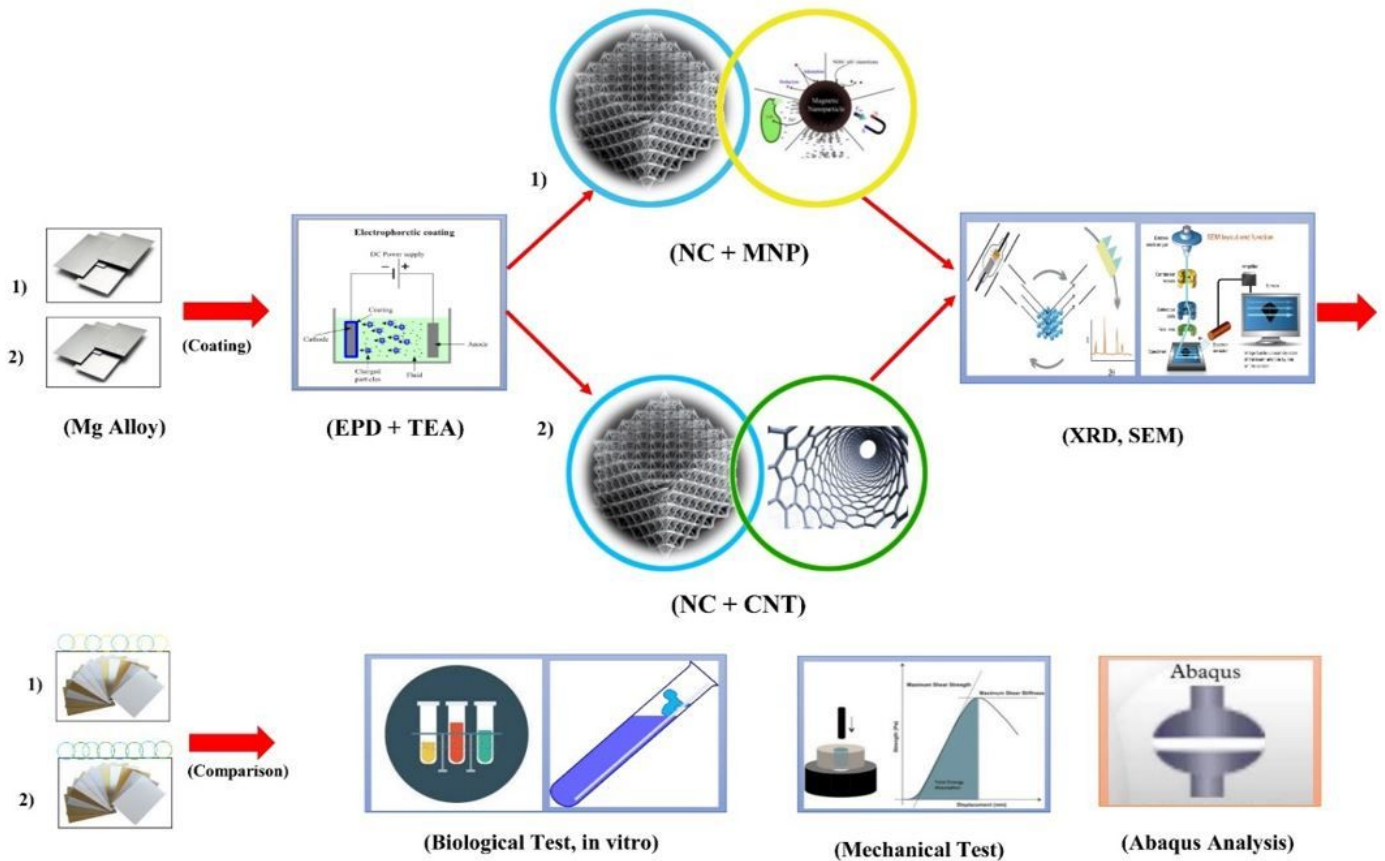


**Figure 1**

Schematic of the process for fabrication of ceramic-magnetic and ceramic-single walled carbon nanotube bio-nanocomposite coated with EPD technique on AZ91 substrate

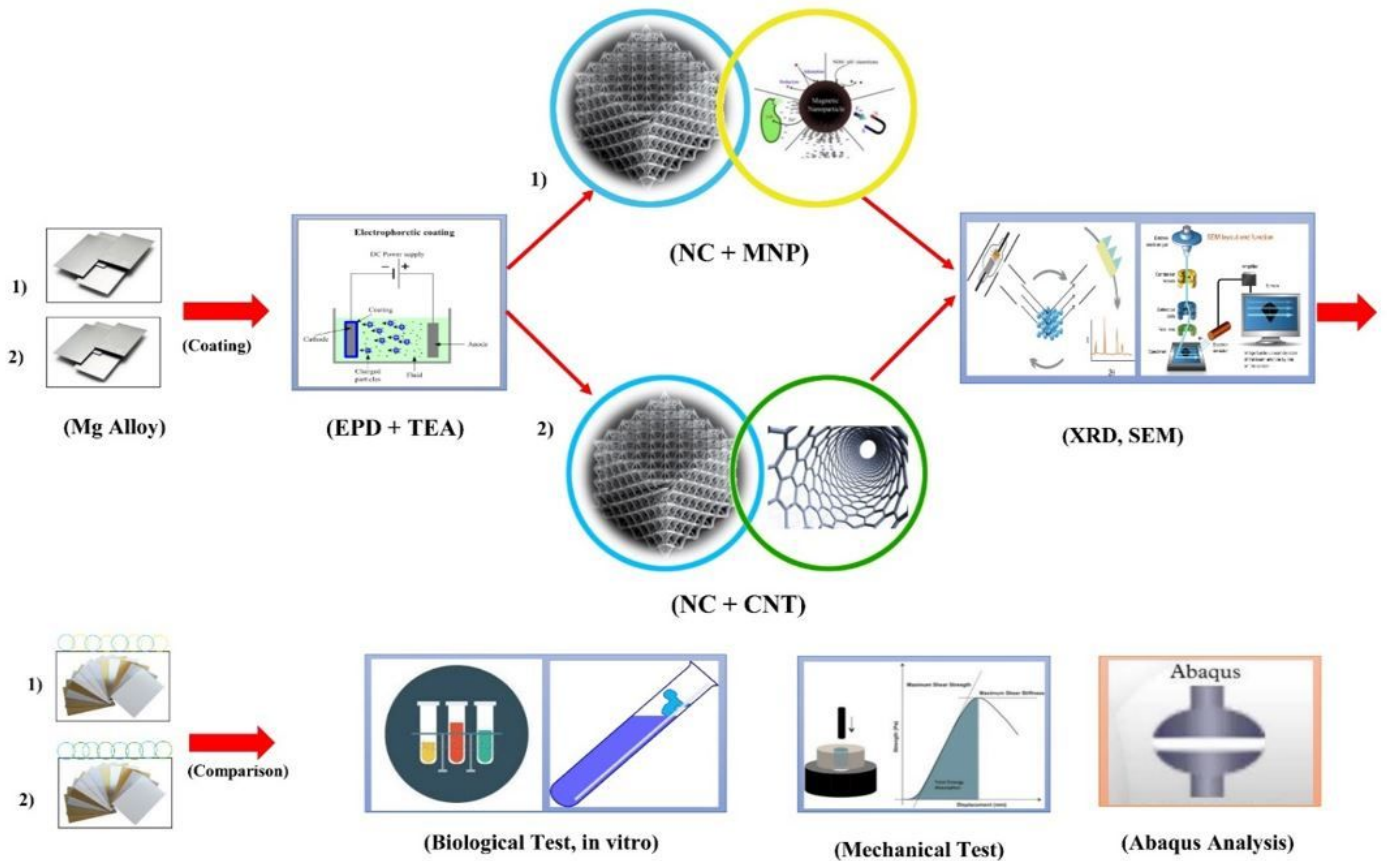


**Figure 1**

Schematic of the process for fabrication of ceramic-magnetic and ceramic-single walled carbon nanotube bio-nanocomposite coated with EPD technique on AZ91 substrate

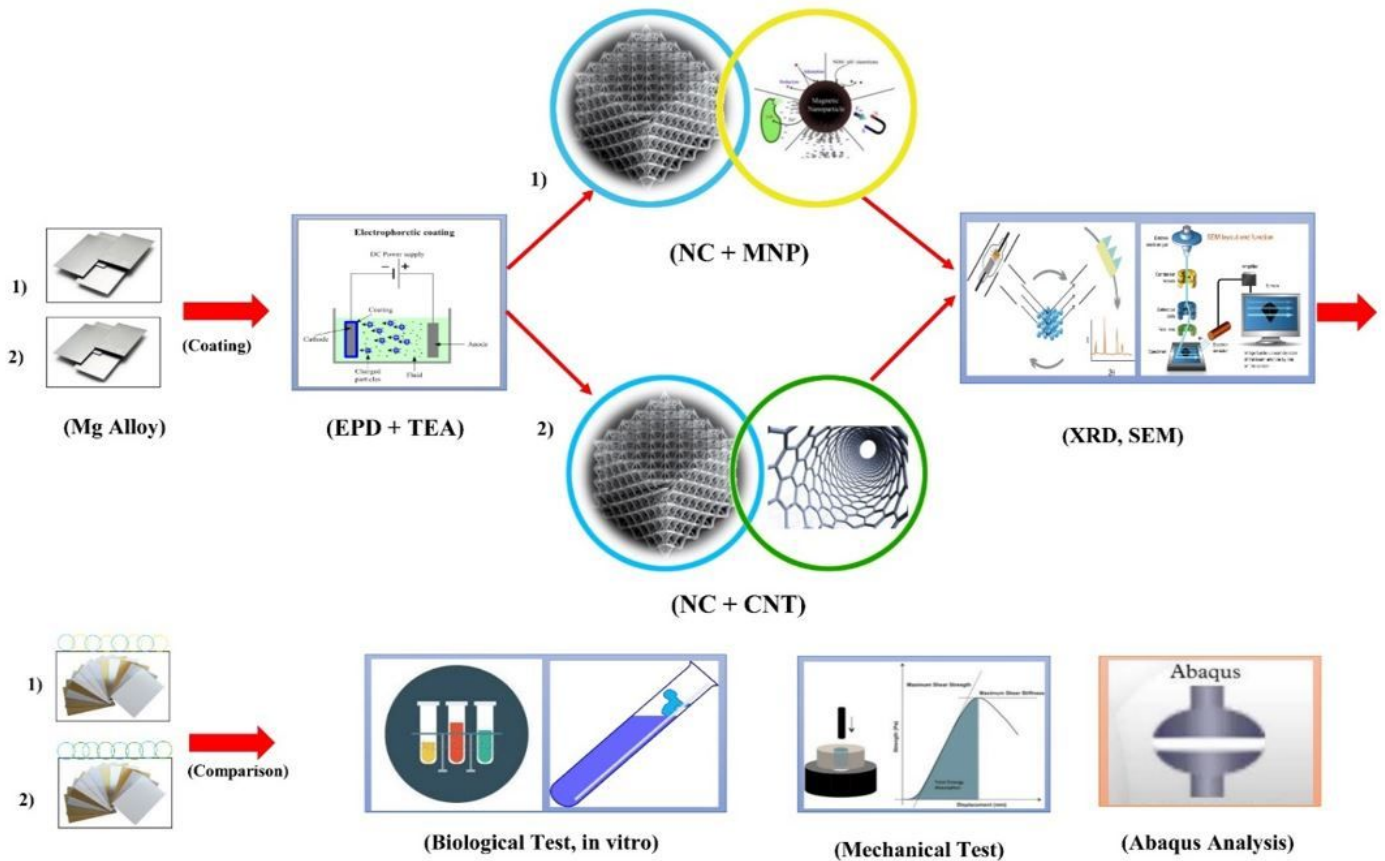


**Figure 1**

Schematic of the process for fabrication of ceramic-magnetic and ceramic-single walled carbon nanotube bio-nanocomposite coated with EPD technique on AZ91 substrate

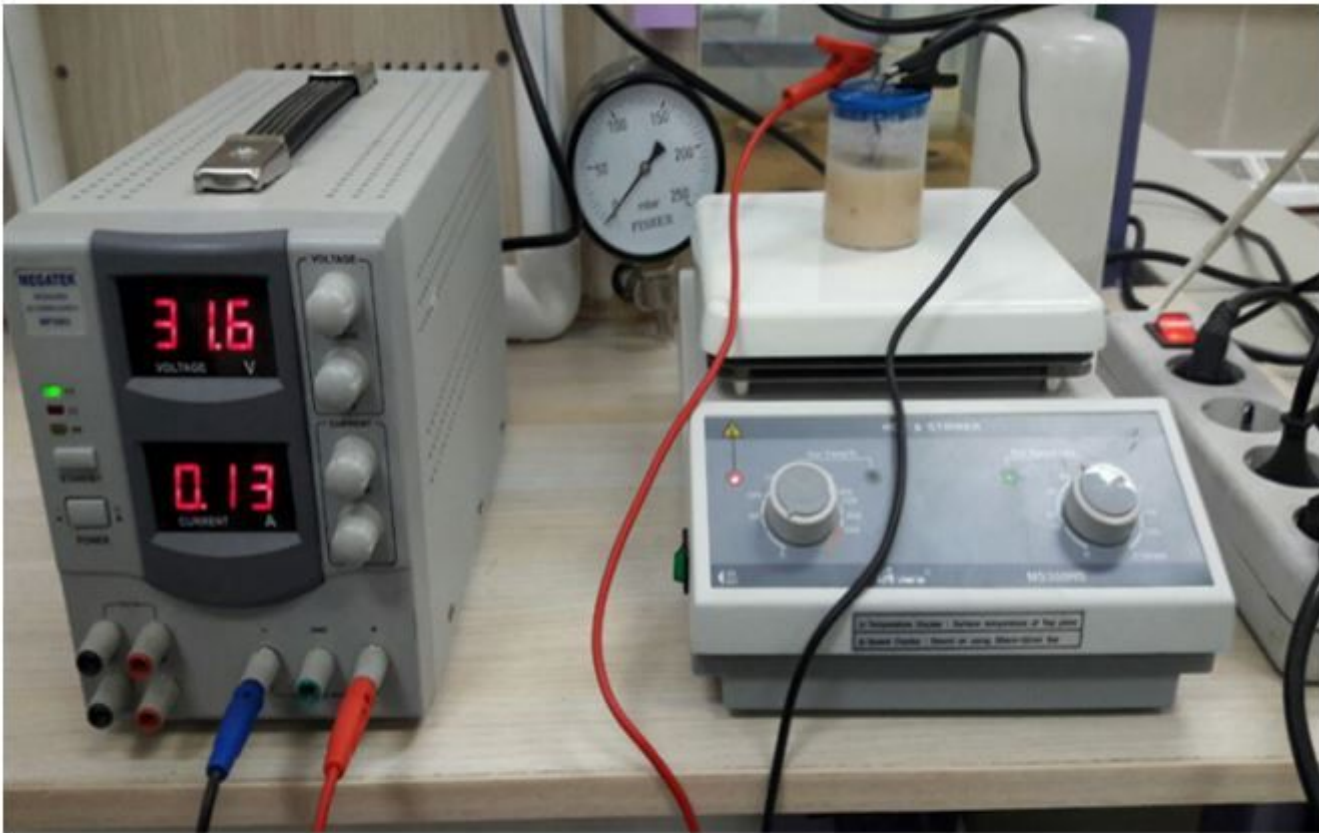


Figure 2

The electrophoretic deposition technique set up for coating of ceramic solution on magnesium substrate.

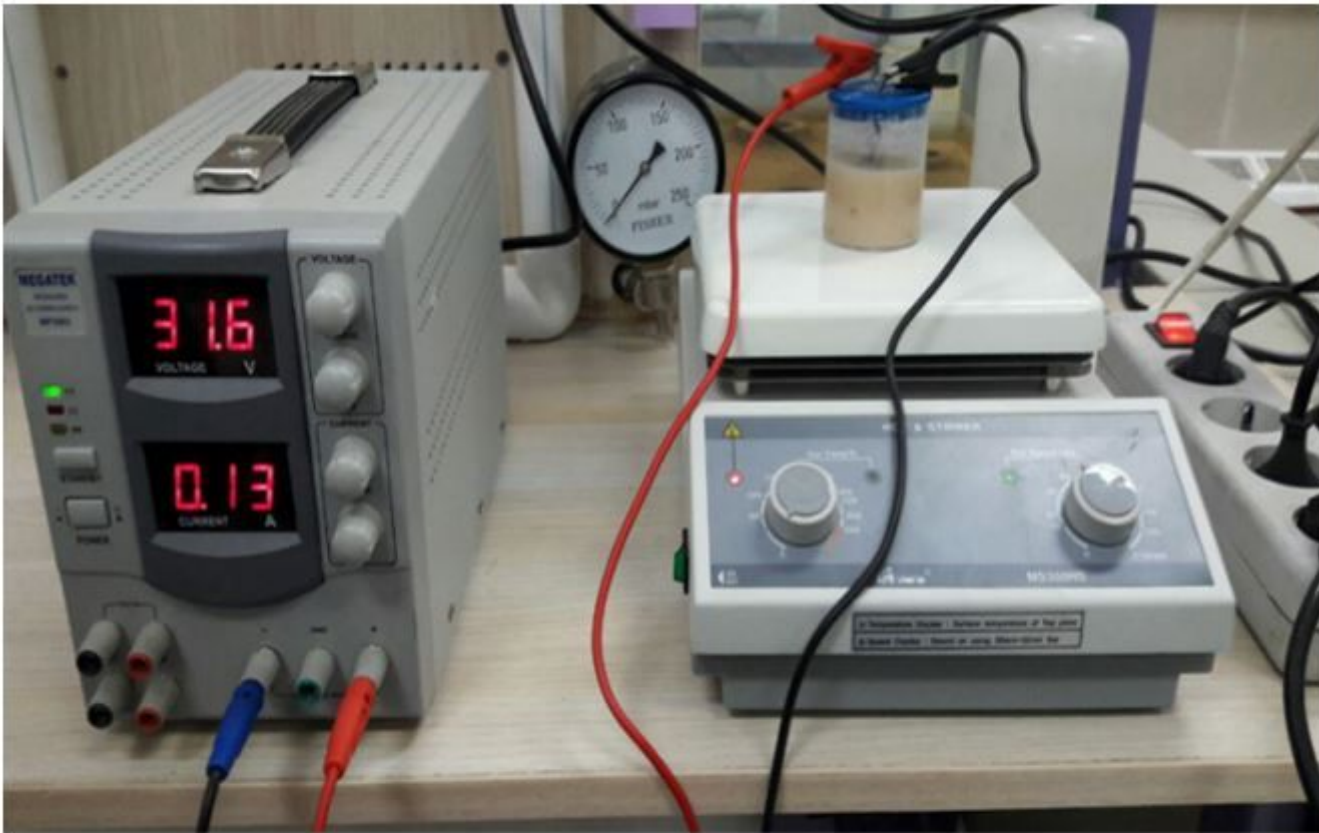


Figure 2

The electrophoretic deposition technique set up for coating of ceramic solution on magnesium substrate.

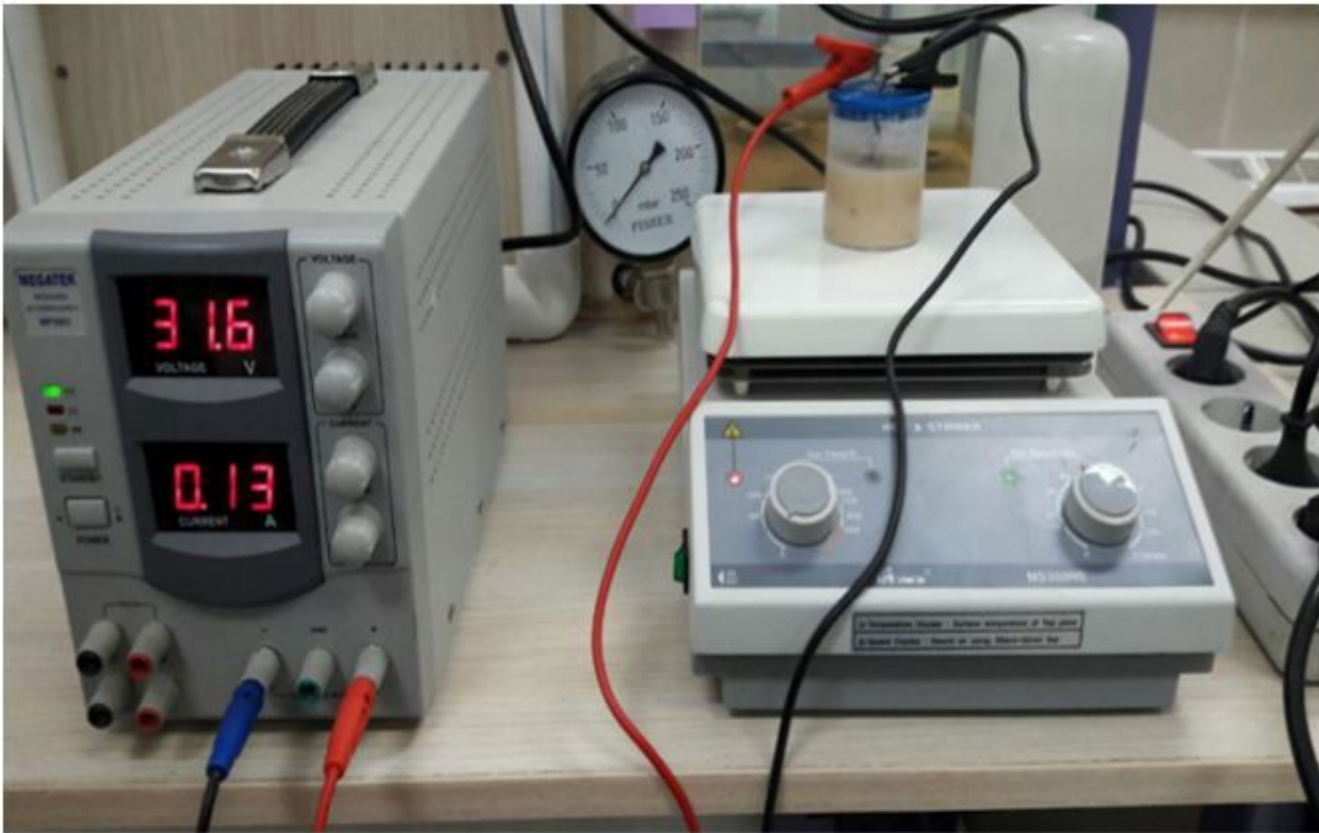
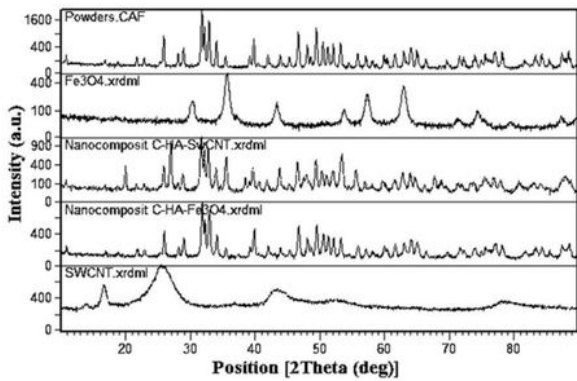
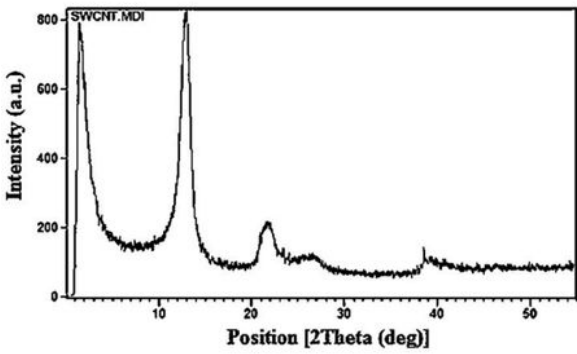
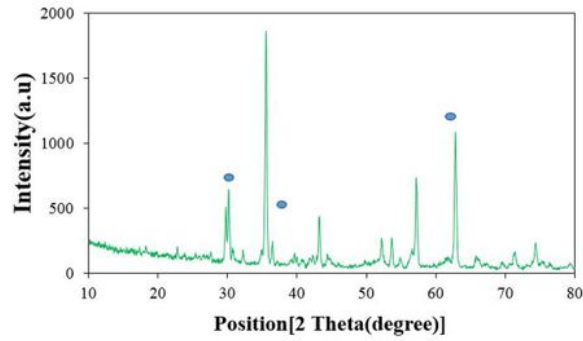
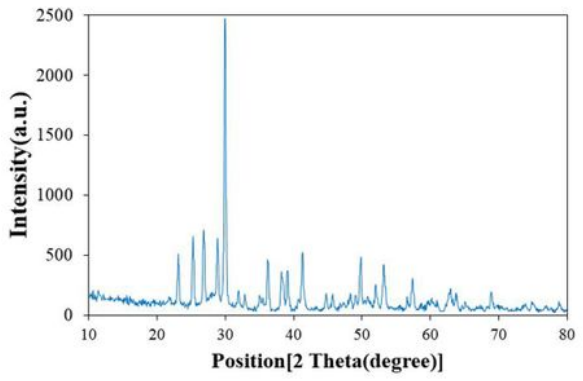


Figure 2

The electrophoretic deposition technique set up for coating of ceramic solution on magnesium substrate.



**Figure 3**

XRD pattern of (a) WS, (b) MNPs, (c) SWCNT, and (d) bio-nanocomposite combination in the range of 10 to 90 degrees

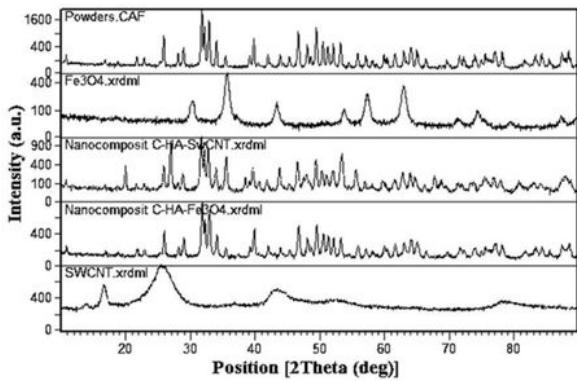
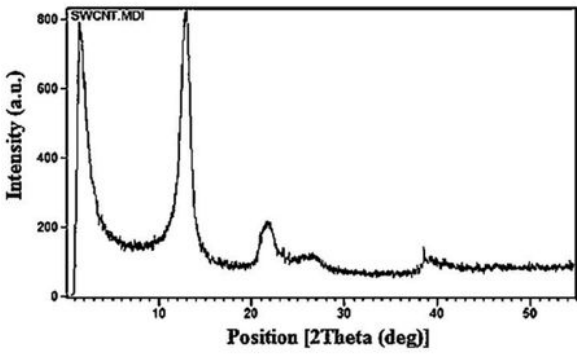
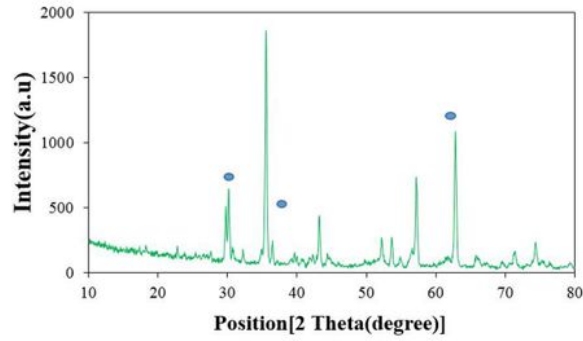
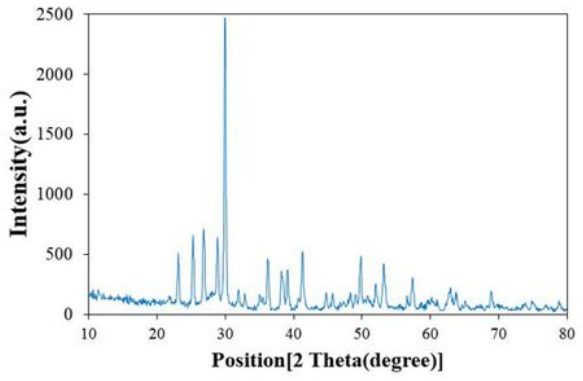


**Figure 3**

XRD pattern of (a) WS, (b) MNPs, (c) SWNT, and (d) bio-nanocomposite combination in the range of 10 to 90 degrees

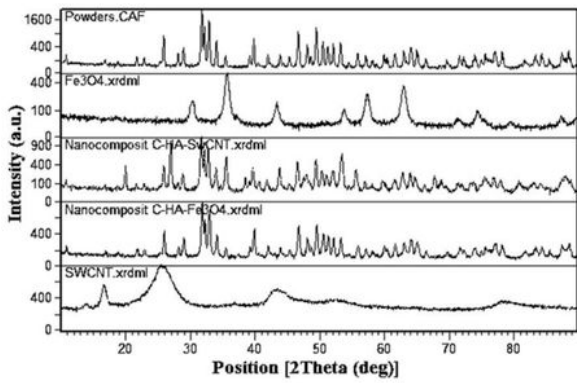
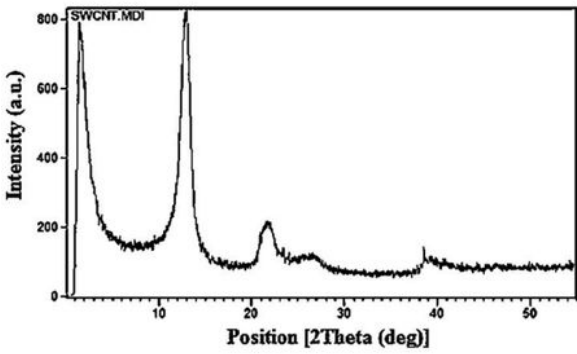
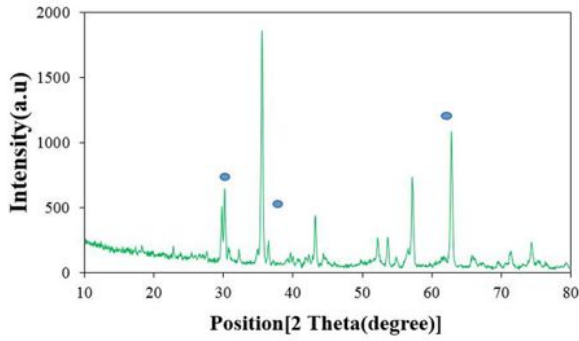
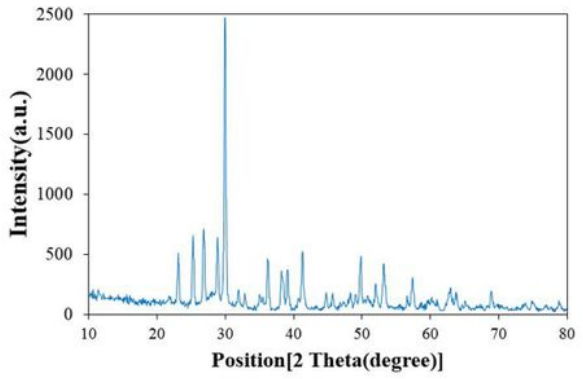


**Figure 3**

XRD pattern of (a) WS, (b) MNPs, (c) SWNT, and (d) bio-nanocomposite combination in the range of 10 to 90 degrees

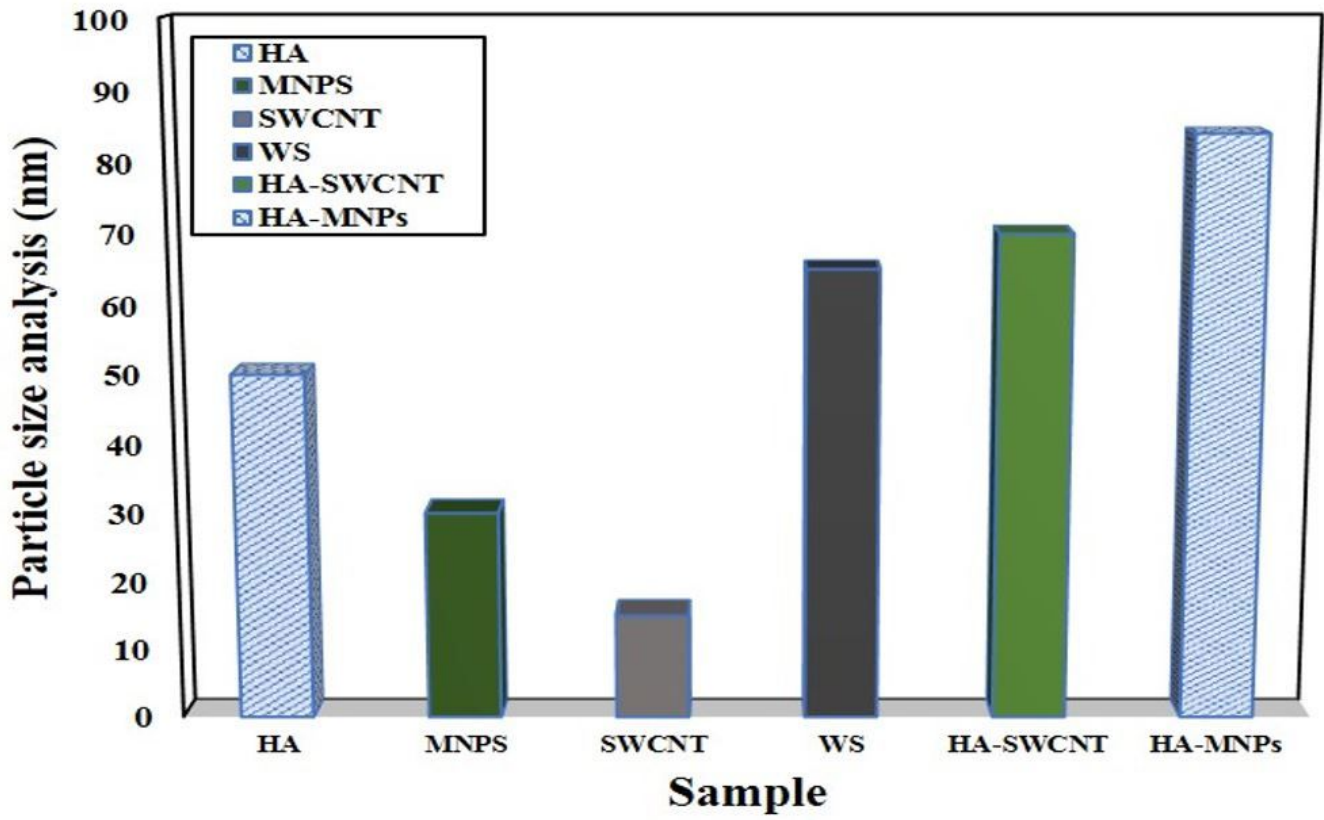


Figure 4

The particle size analysis of WS, MNPs, SWNT, and bio-nanocomposite

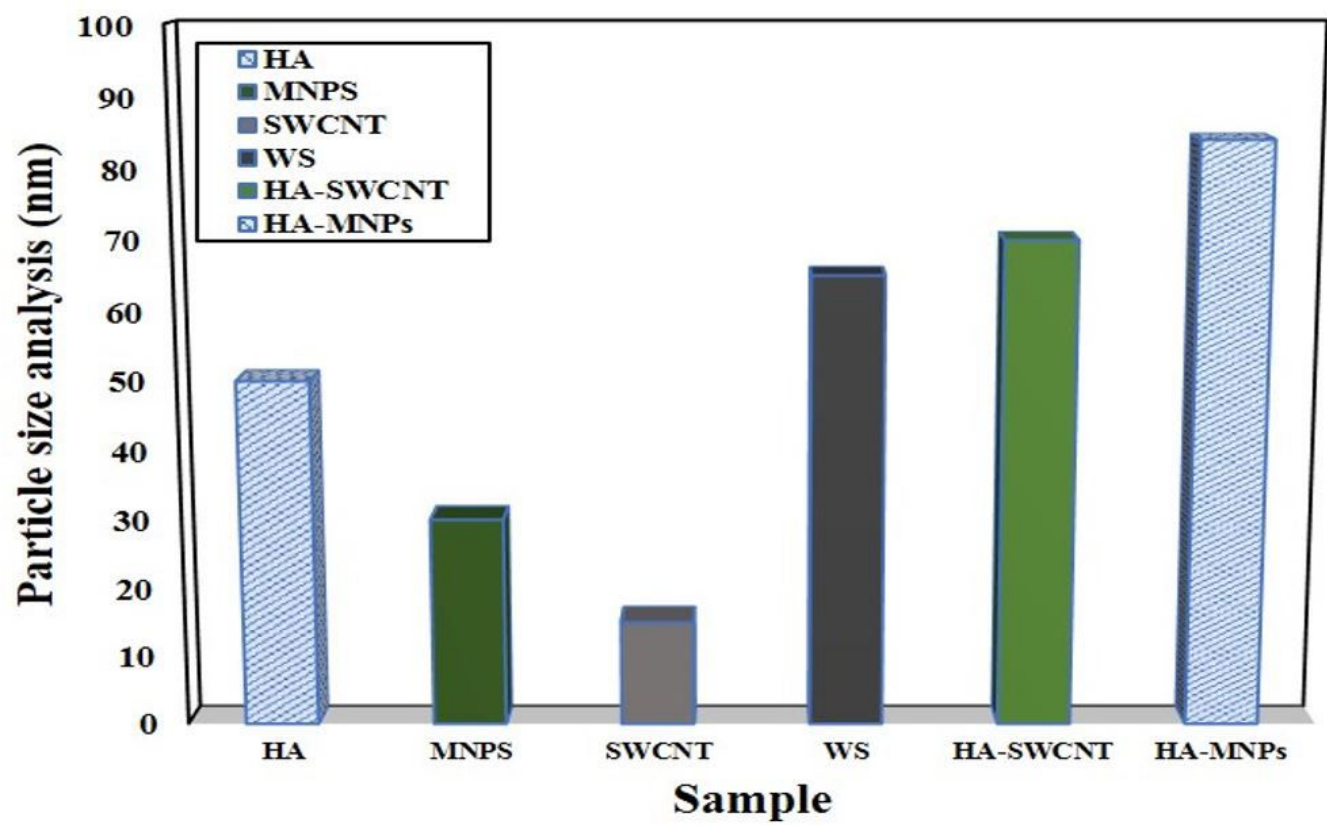


Figure 4

The particle size analysis of WS, MNPs, SWNT, and bio-nanocomposite

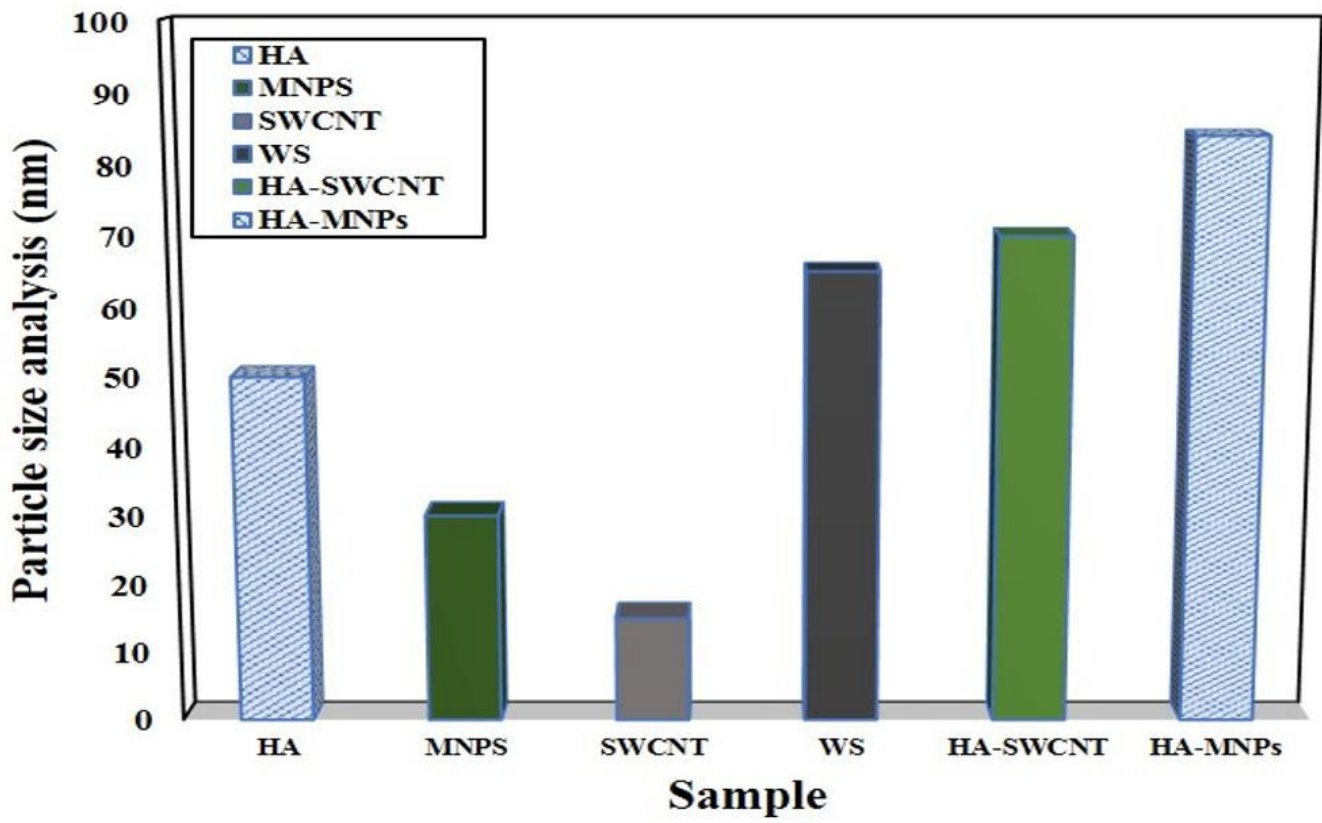
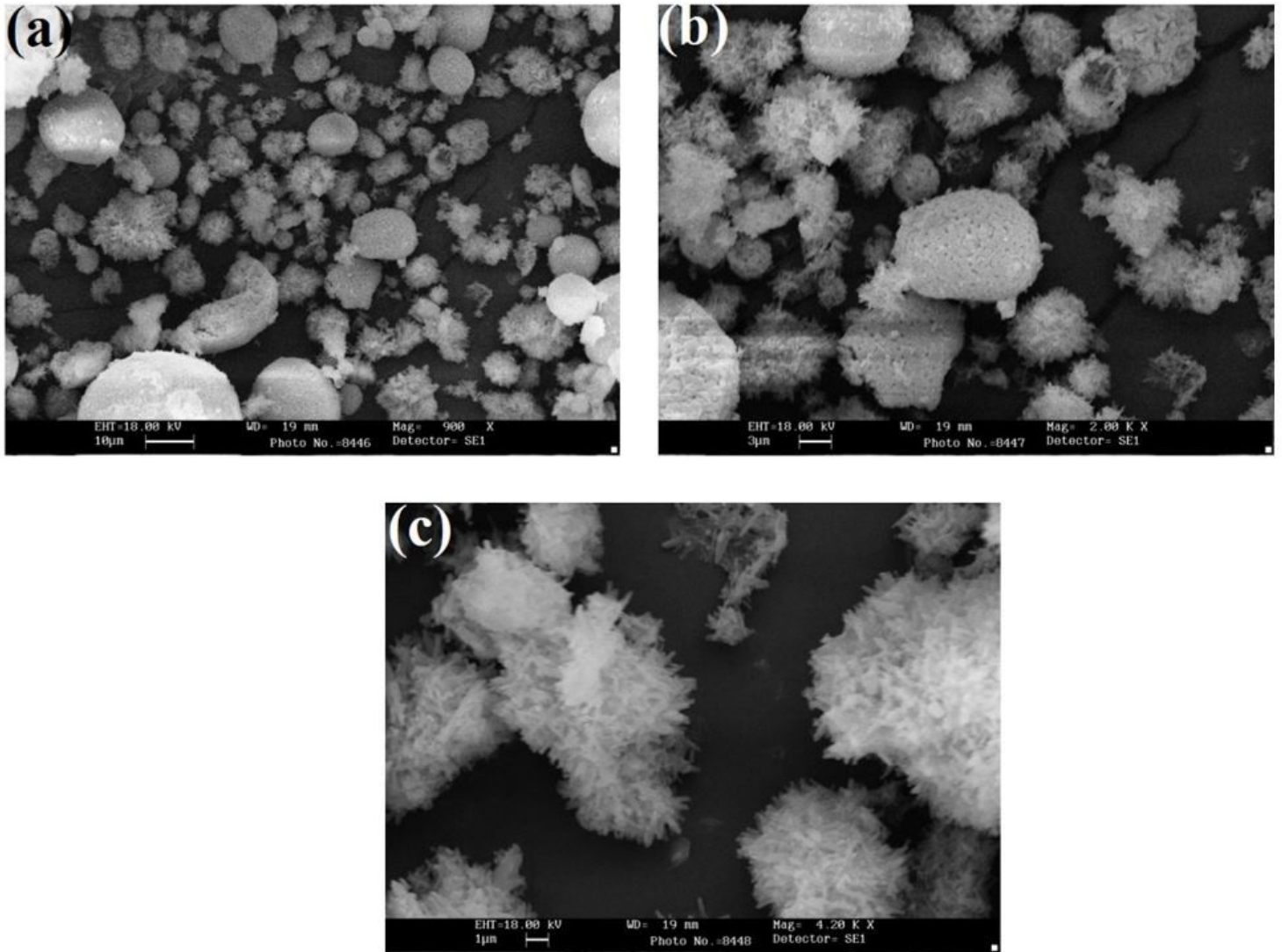


Figure 4

The particle size analysis of WS, MNPs, SWNT, and bio-nanocomposite



**Figure 5**

SEM images of (a) hydroxyapatite powder, (b) synthesized wollastonite, (c) hydroxyapatite-wollastonite nanopowder

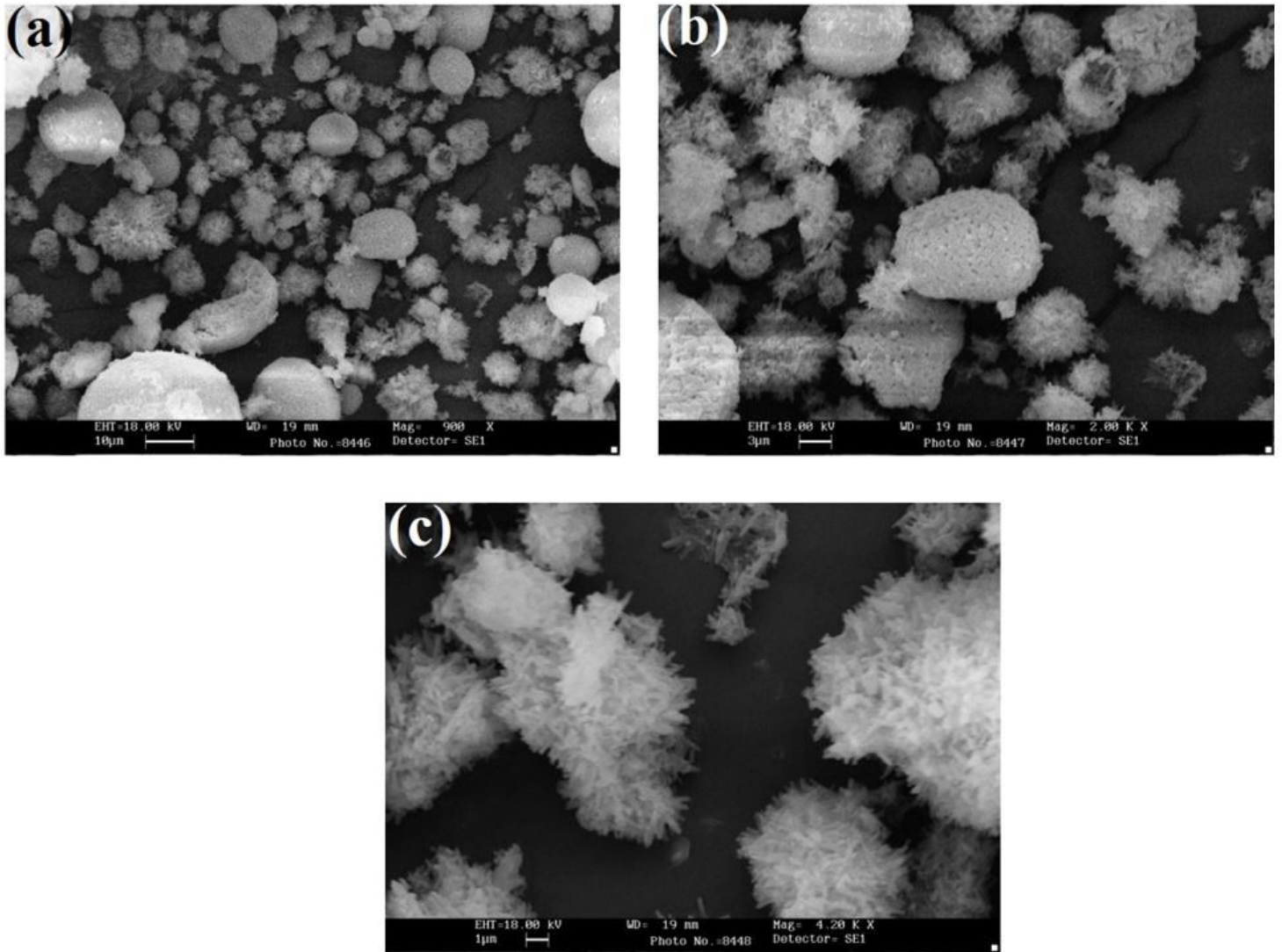


**Figure 5**

SEM images of (a) hydroxyapatite powder, (b) synthesized wollastonite, (c) hydroxyapatite-wollastonite nanopowder

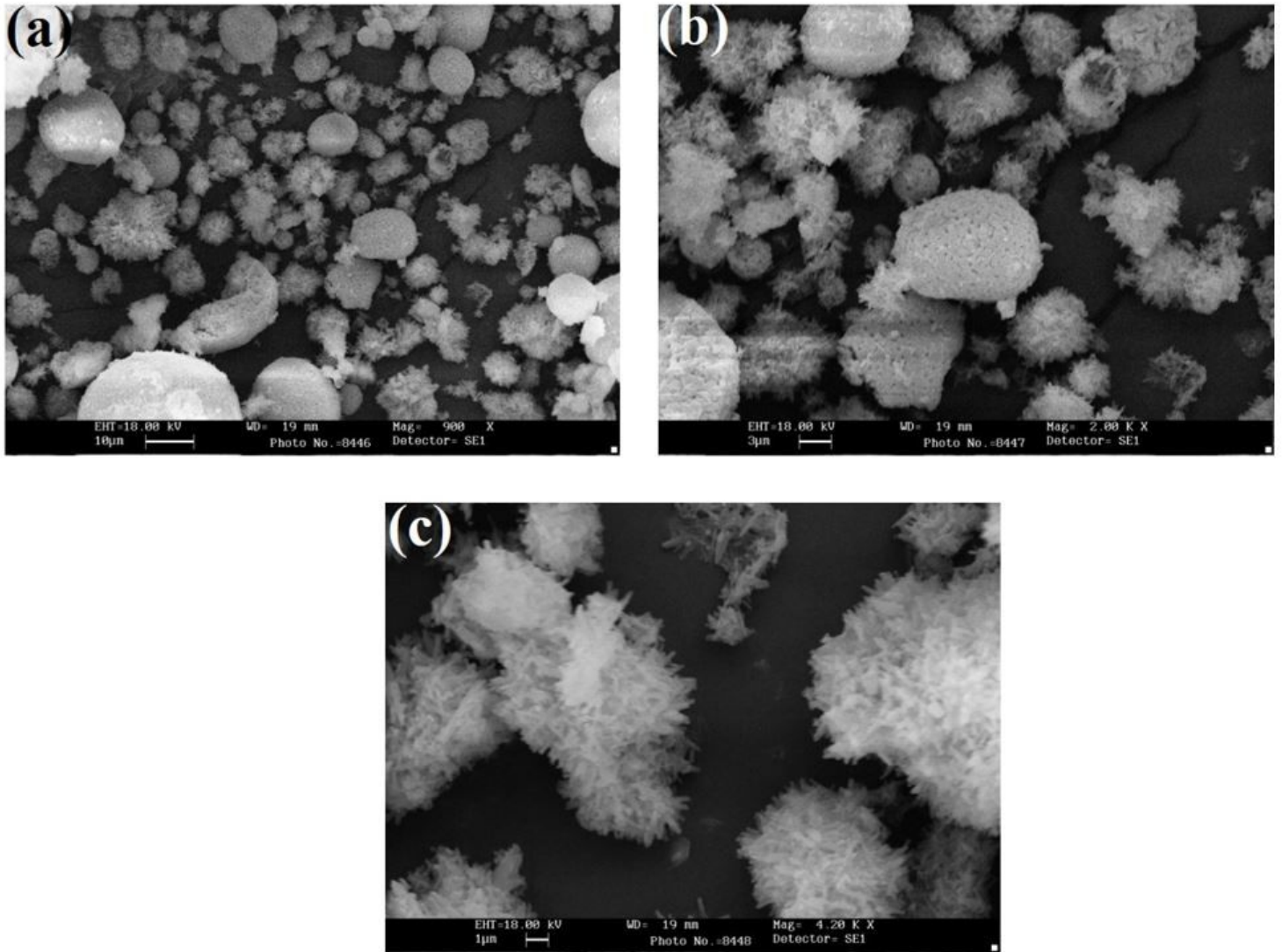


**Figure 5**

SEM images of (a) hydroxyapatite powder, (b) synthesized wollastonite, (c) hydroxyapatite-wollastonite nanopowder

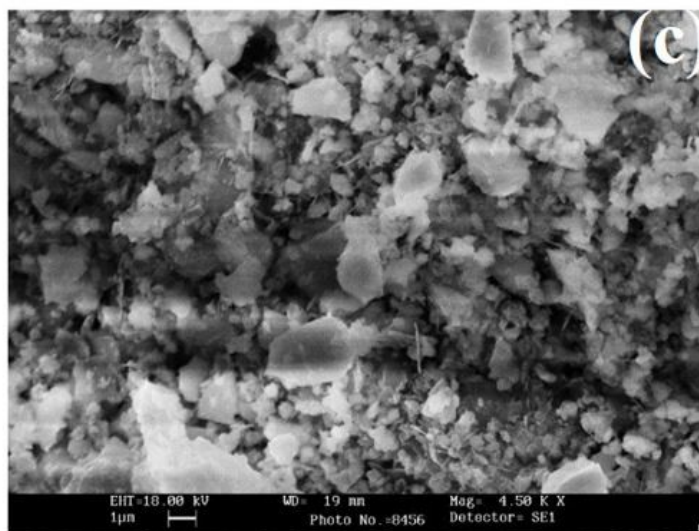
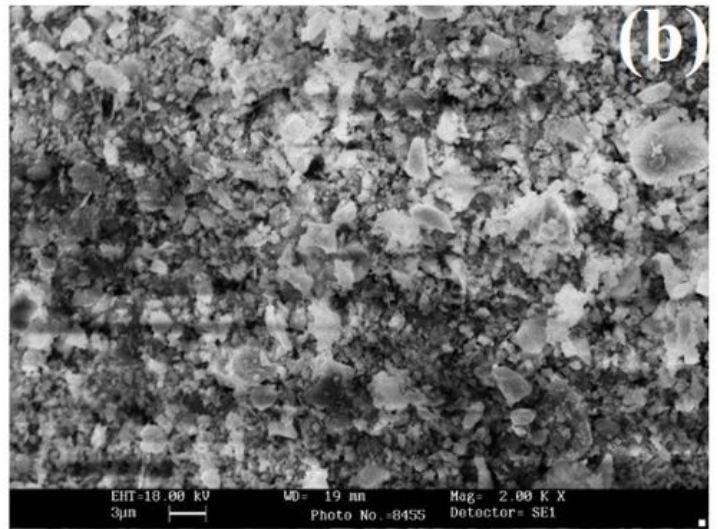
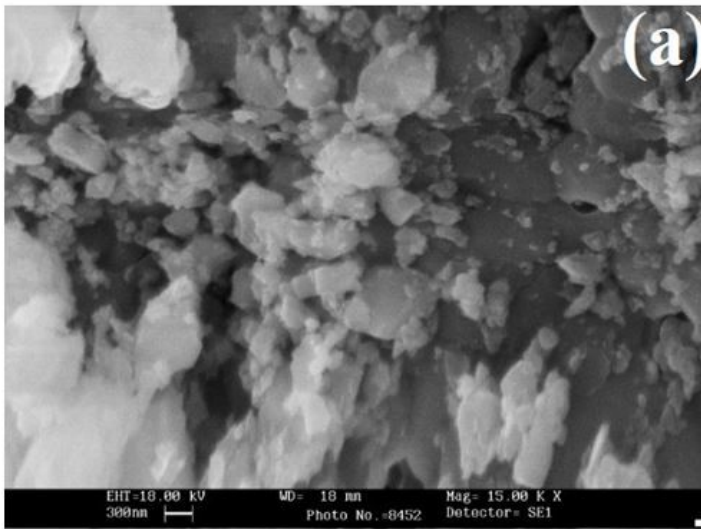


**Figure 6**

SEM images of (a) hydroxyapatite-wollastonite bio-nanocomposite powders, (b) hydroxyapatite-wollastonite-magnetite nanoparticle bio-nanocomposite, (c) hydroxyapatite-wollastonite-single walled carbon nanotube bio-nanocomposite

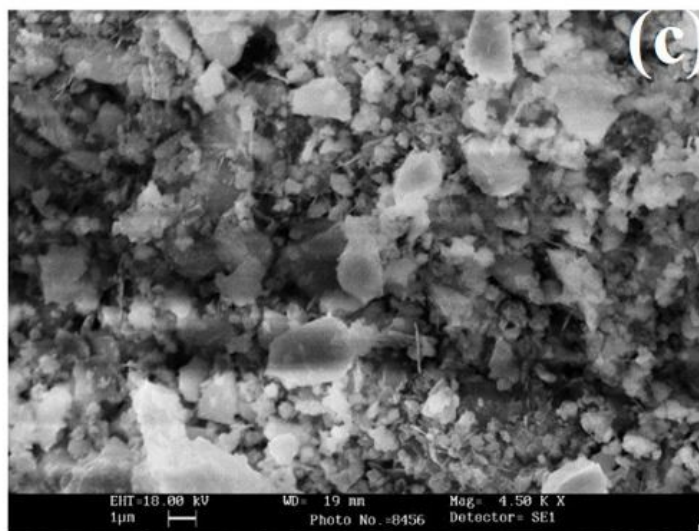
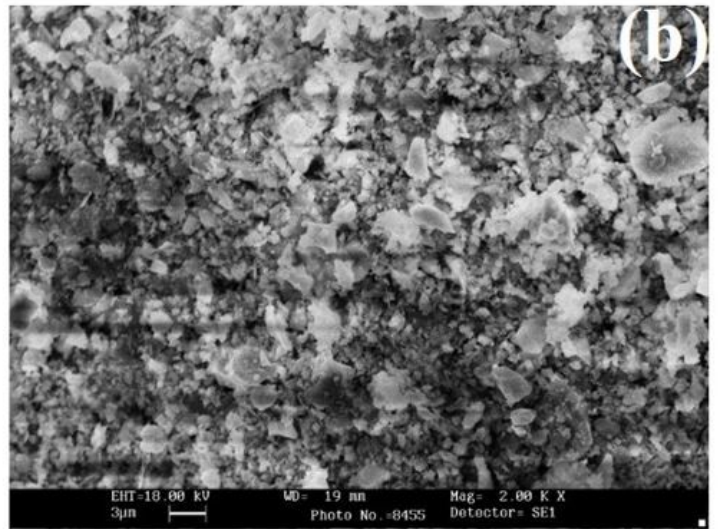
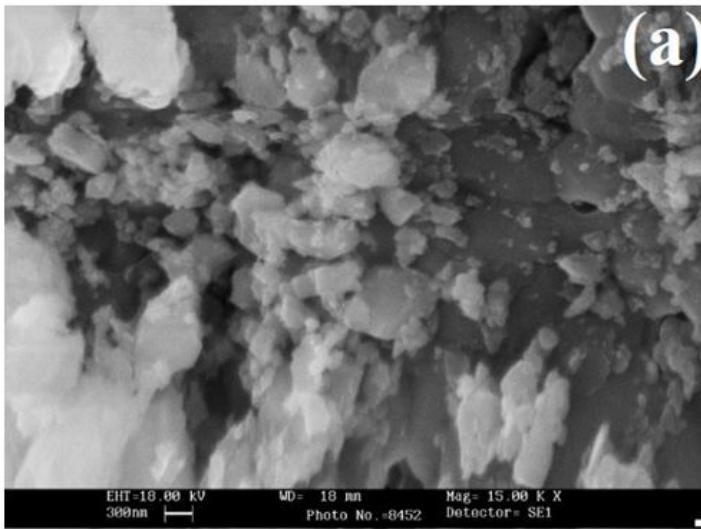


**Figure 6**

SEM images of (a) hydroxyapatite-wollastonite bio-nanocomposite powders, (b) hydroxyapatite-wollastonite-magnetite nanoparticle bio-nanocomposite, (c) hydroxyapatite-wollastonite-single walled carbon nanotube bio-nanocomposite

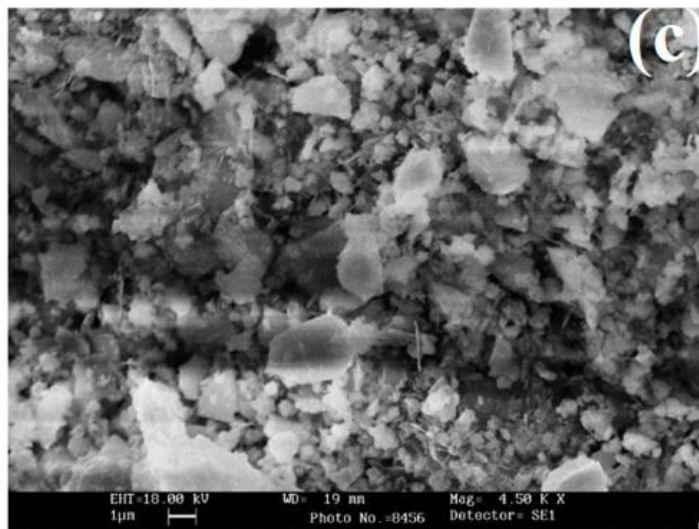
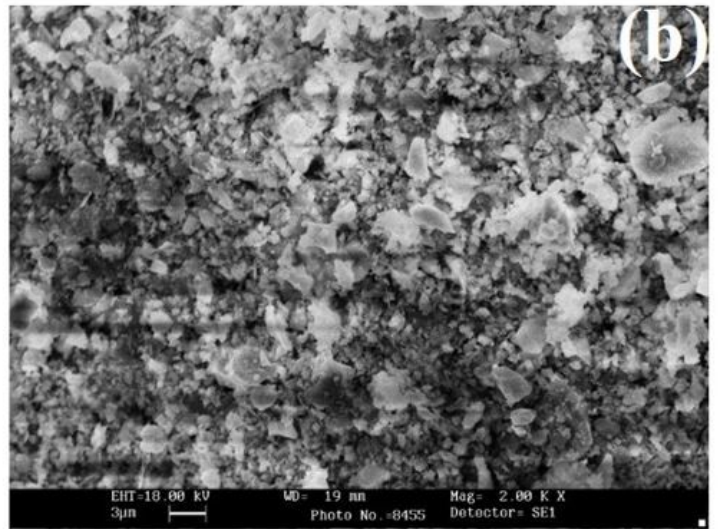
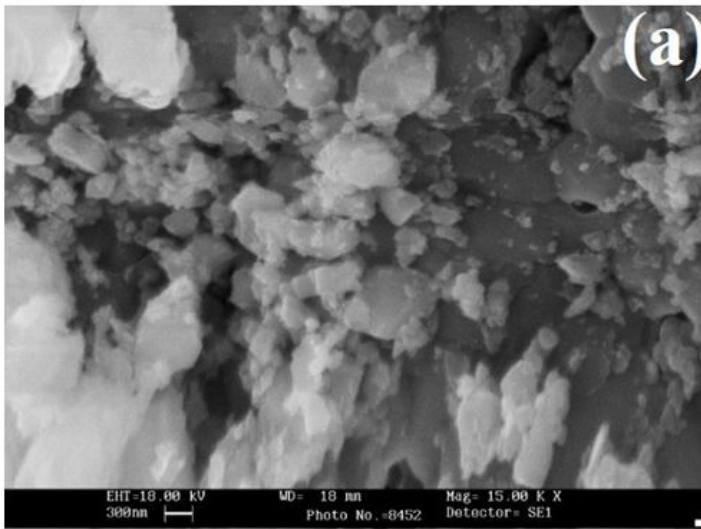


**Figure 6**

SEM images of (a) hydroxyapatite-wollastonite bio-nanocomposite powders, (b) hydroxyapatite-wollastonite-magnetite nanoparticle bio-nanocomposite, (c) hydroxyapatite-wollastonite-single walled carbon nanotube bio-nanocomposite

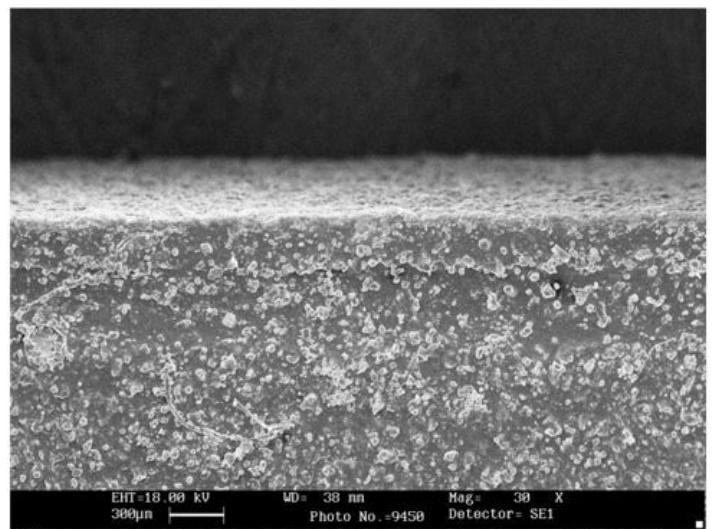
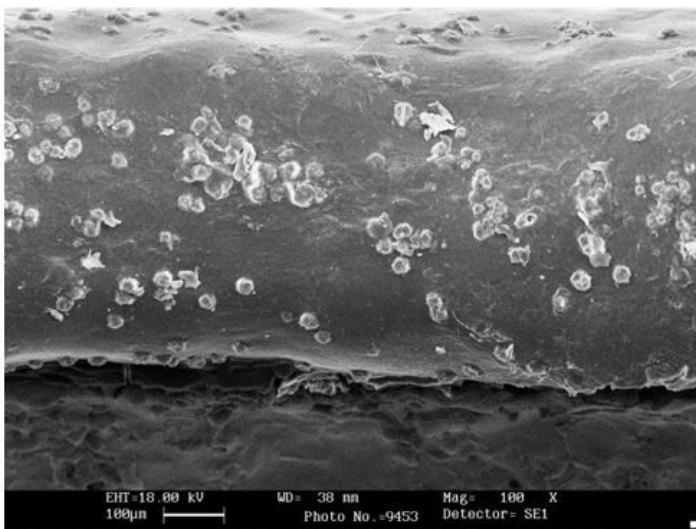
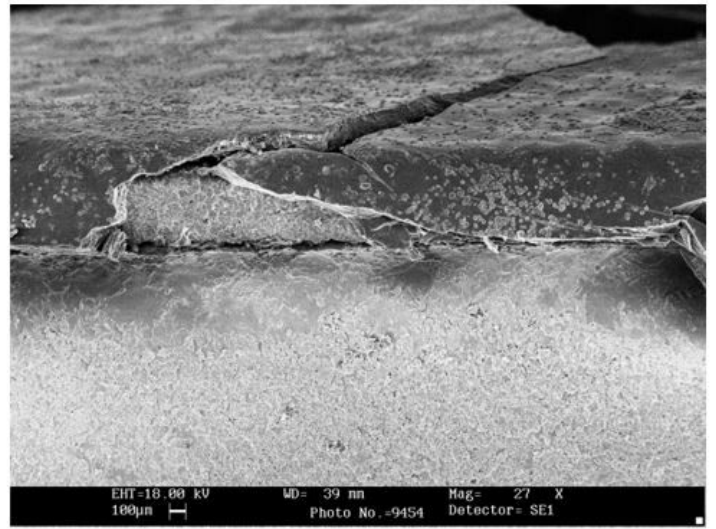
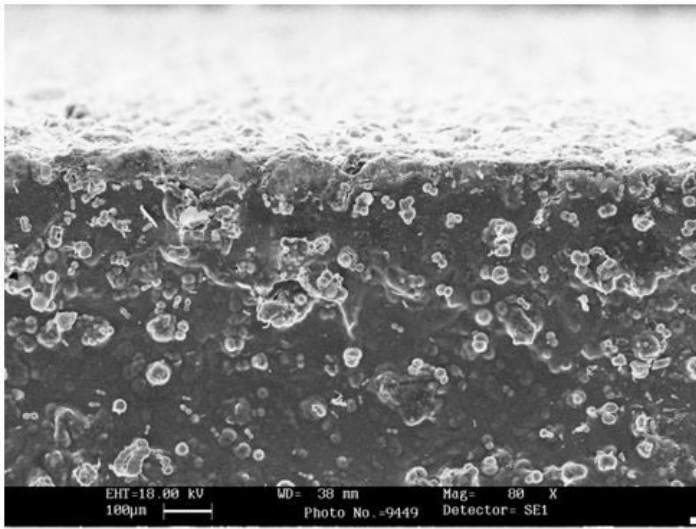


**Figure 7**

SEM images of cross section surface of (a) hydroxyapatite-wollastonite bio-nanocomposite, (b) hydroxyapatite-wollastonite-single walled carbon nanotube bio-nanocomposite, (c) hydroxyapatite-wollastonite-magnetic nanoparticle coating taken after soaking the sample in SBF solution for 28 days

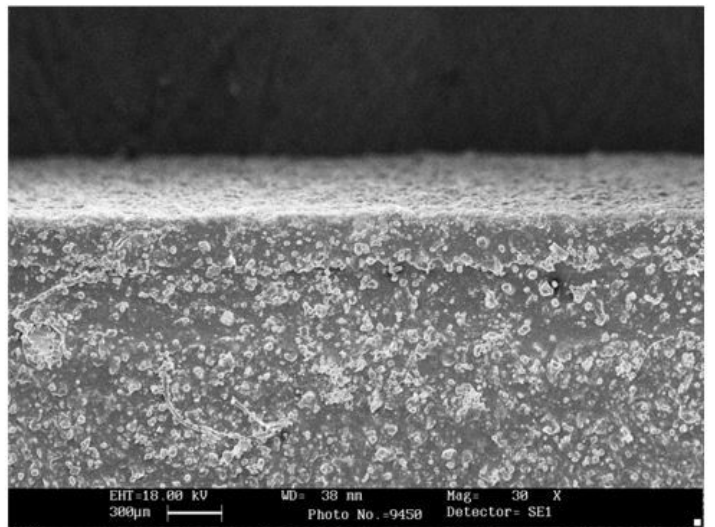
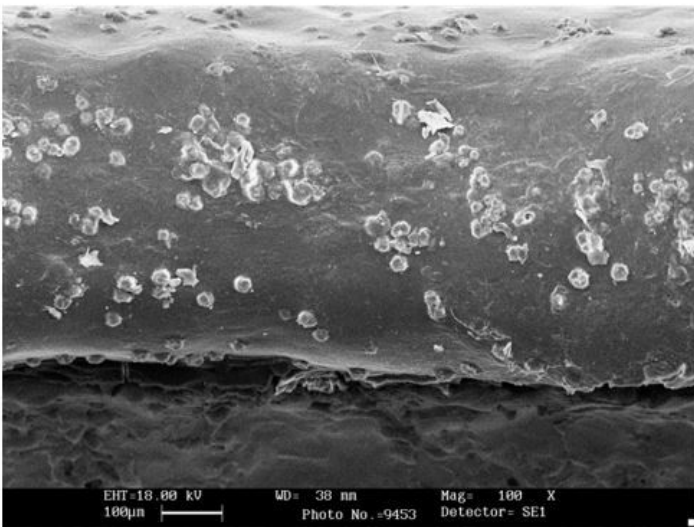
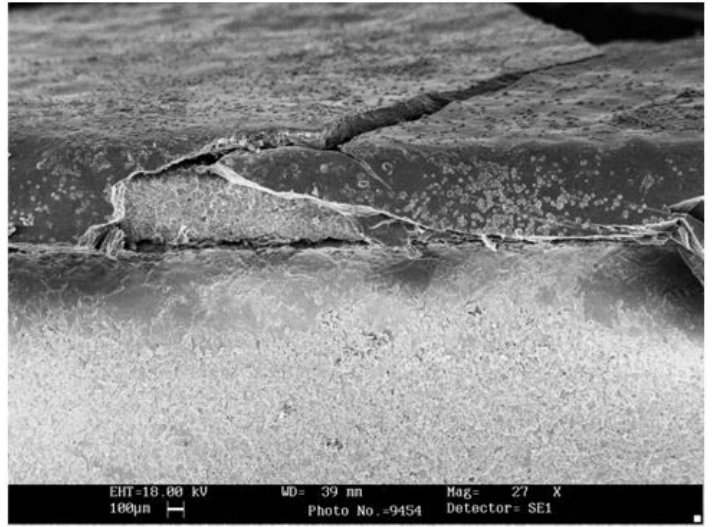
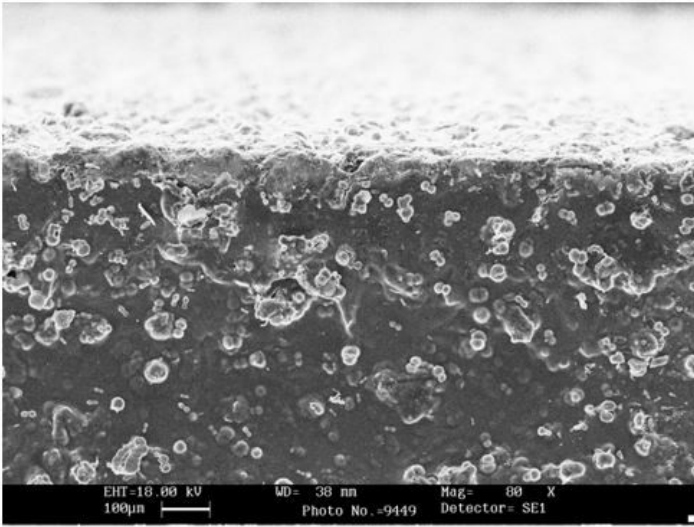


**Figure 7**

SEM images of cross section surface of (a) hydroxyapatite-wollastonite bio-nanocomposite, (b) hydroxyapatite-wollastonite-single walled carbon nanotube bio-nanocomposite, (c) hydroxyapatite-wollastonite-magnetic nanoparticle coating taken after soaking the sample in SBF solution for 28 days

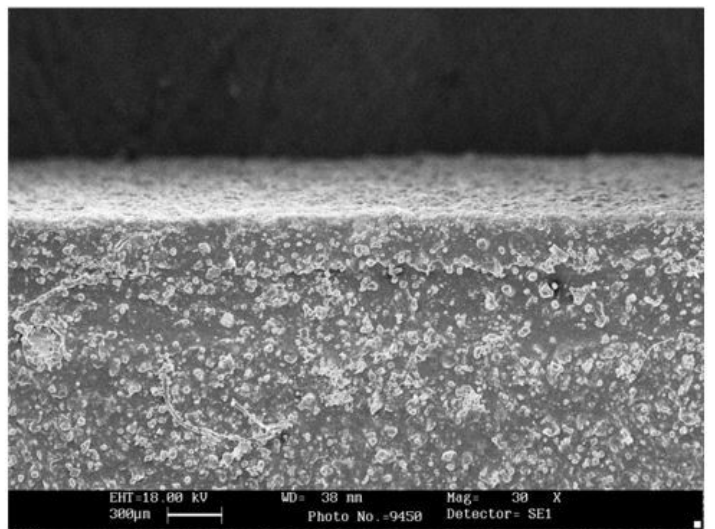
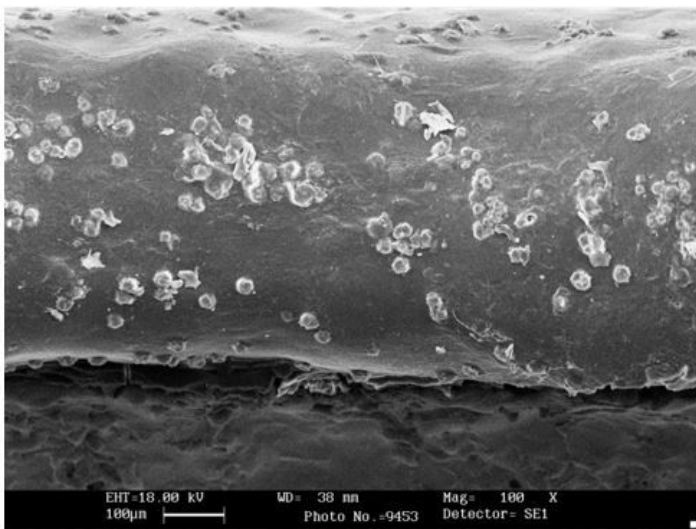
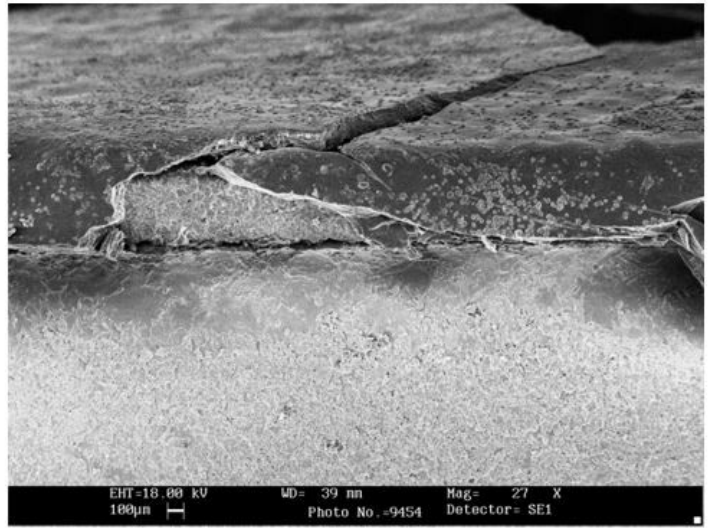
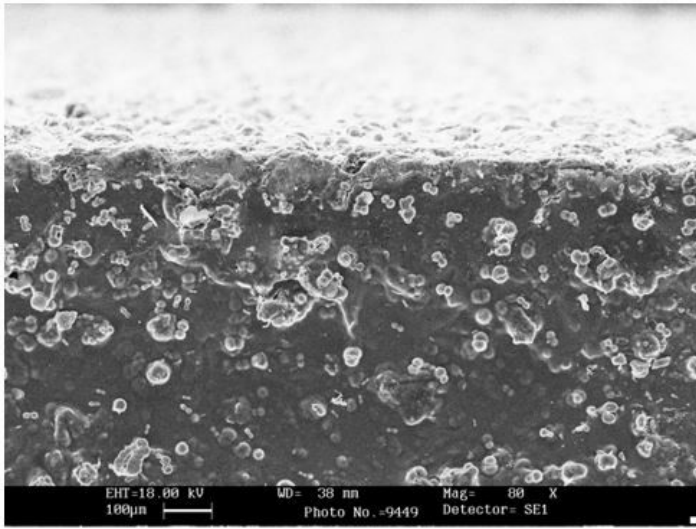


**Figure 7**

SEM images of cross section surface of (a) hydroxyapatite-wollastonite bio-nanocomposite, (b) hydroxyapatite-wollastonite-single walled carbon nanotube bio-nanocomposite, (c) hydroxyapatite-wollastonite-magnetic nanoparticle coating taken after soaking the sample in SBF solution for 28 days

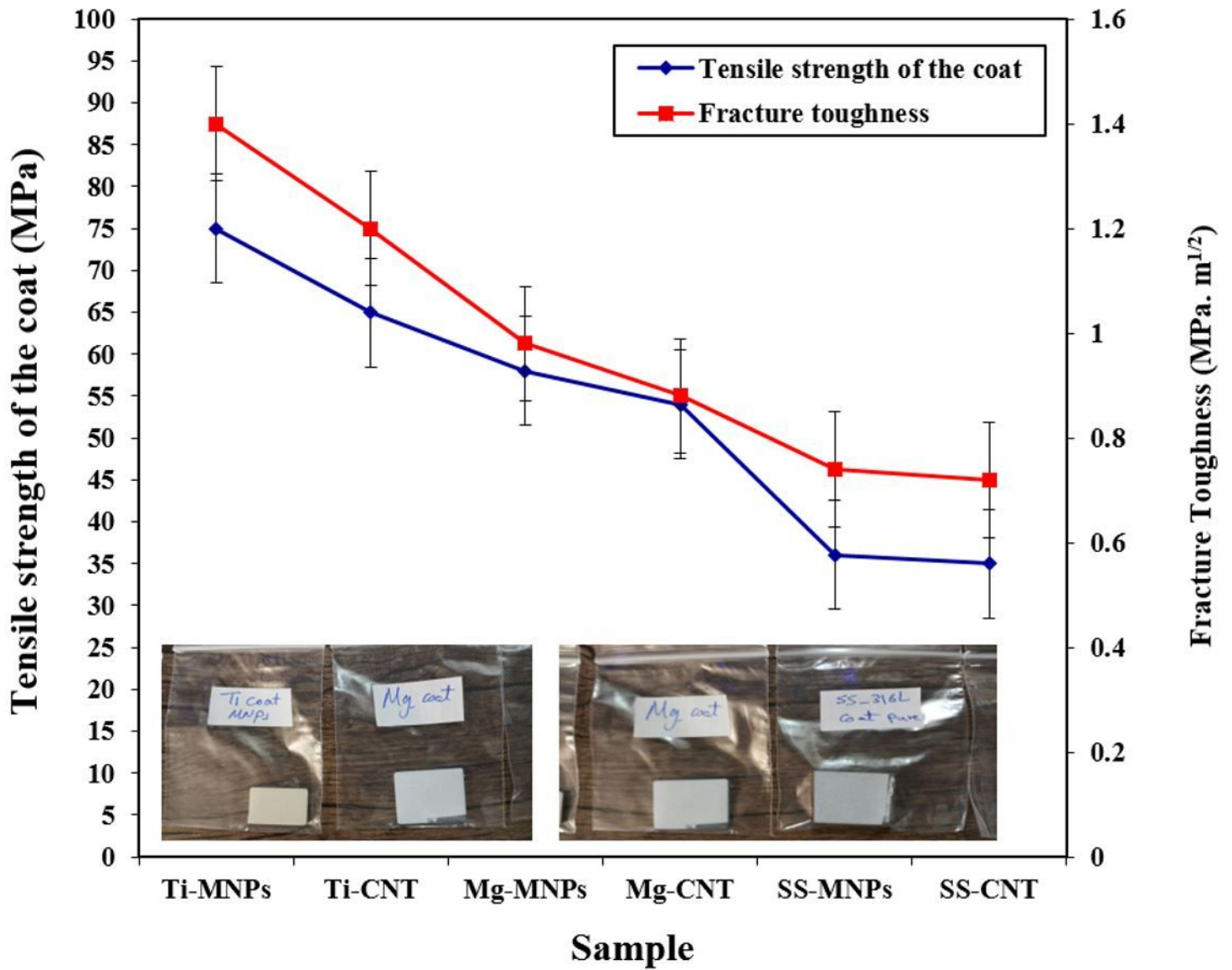


Figure 8

Diagrams of tensile strength and fracture toughness of porous coatings of different samples with magnetic reinforcing nanoparticles and carbon nanotubes on titanium, magnesium and stainless-steel alloys

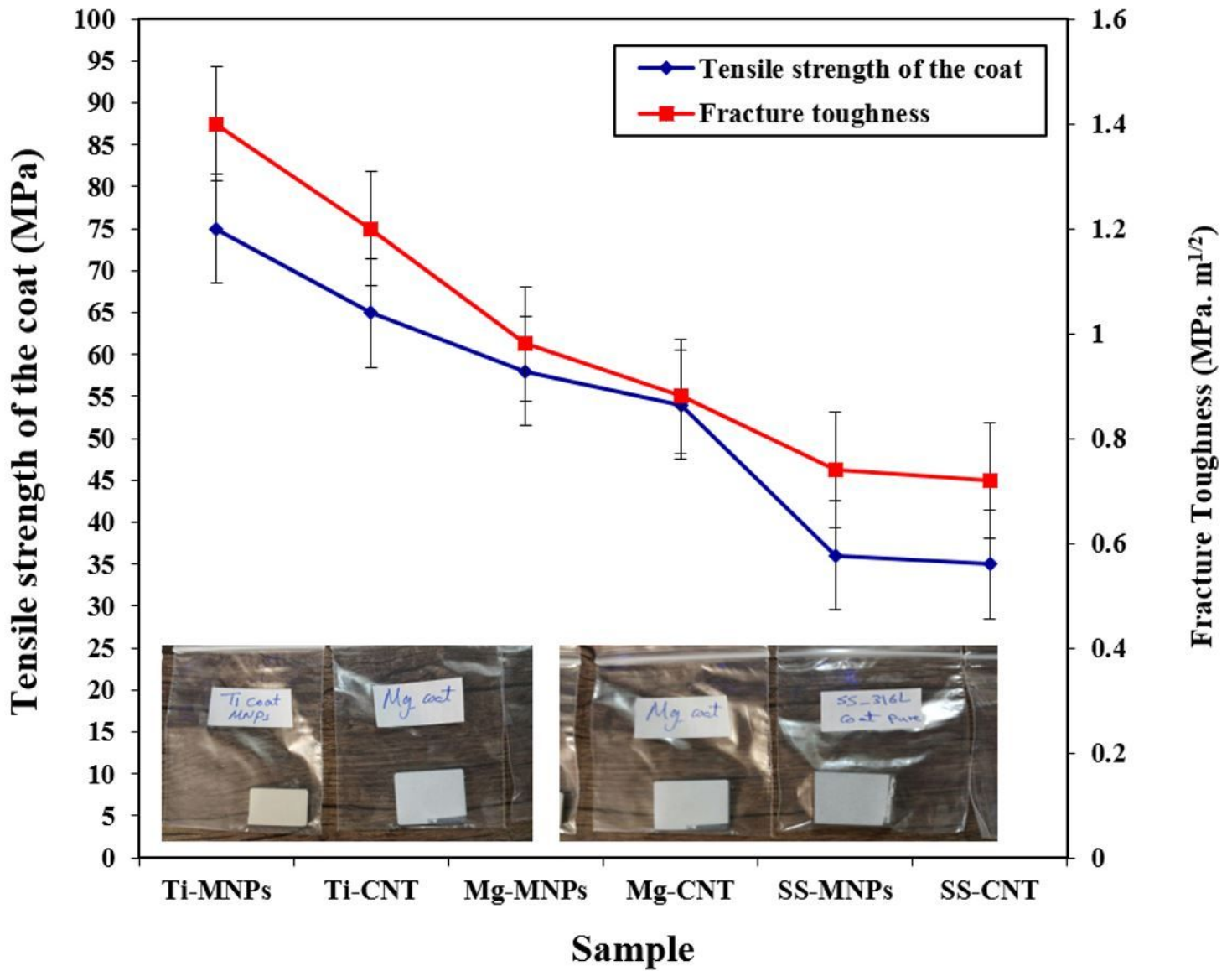


Figure 8

Diagrams of tensile strength and fracture toughness of porous coatings of different samples with magnetic reinforcing nanoparticles and carbon nanotubes on titanium, magnesium and stainless-steel alloys

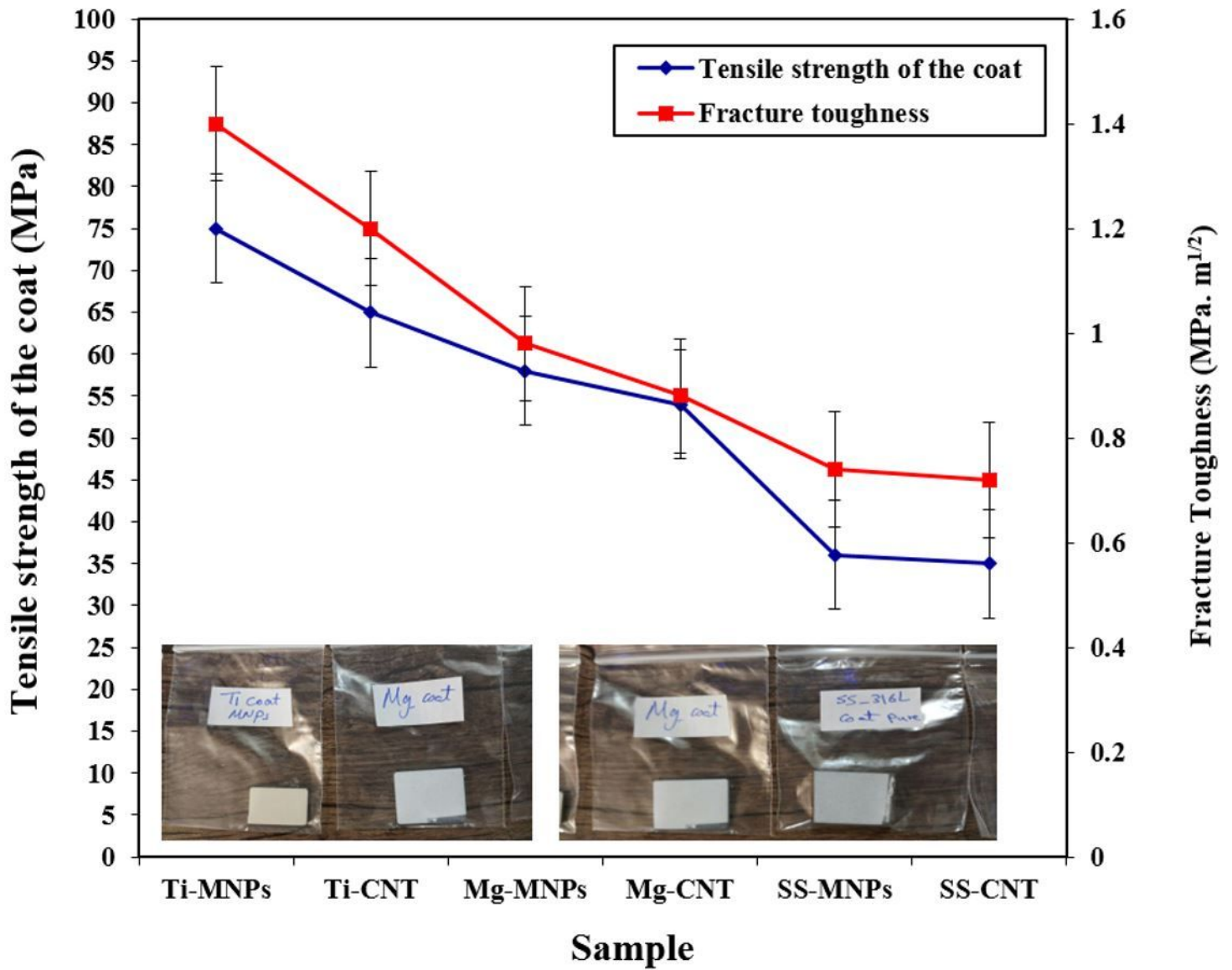


Figure 8

Diagrams of tensile strength and fracture toughness of porous coatings of different samples with magnetic reinforcing nanoparticles and carbon nanotubes on titanium, magnesium and stainless-steel alloys

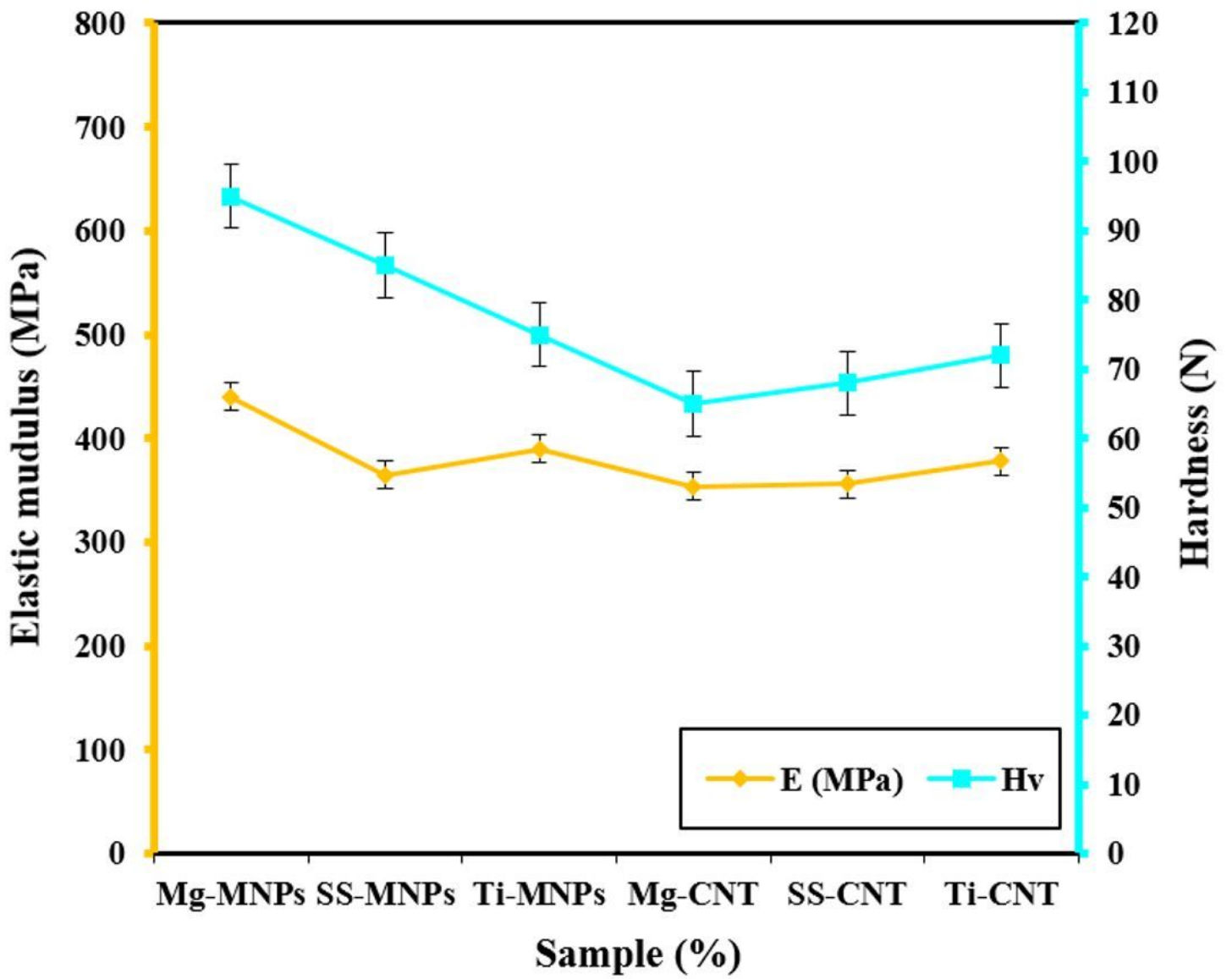


Figure 9

Results of the strength modulus comparison of micro hardness coatings on different alloys by nano-induction device

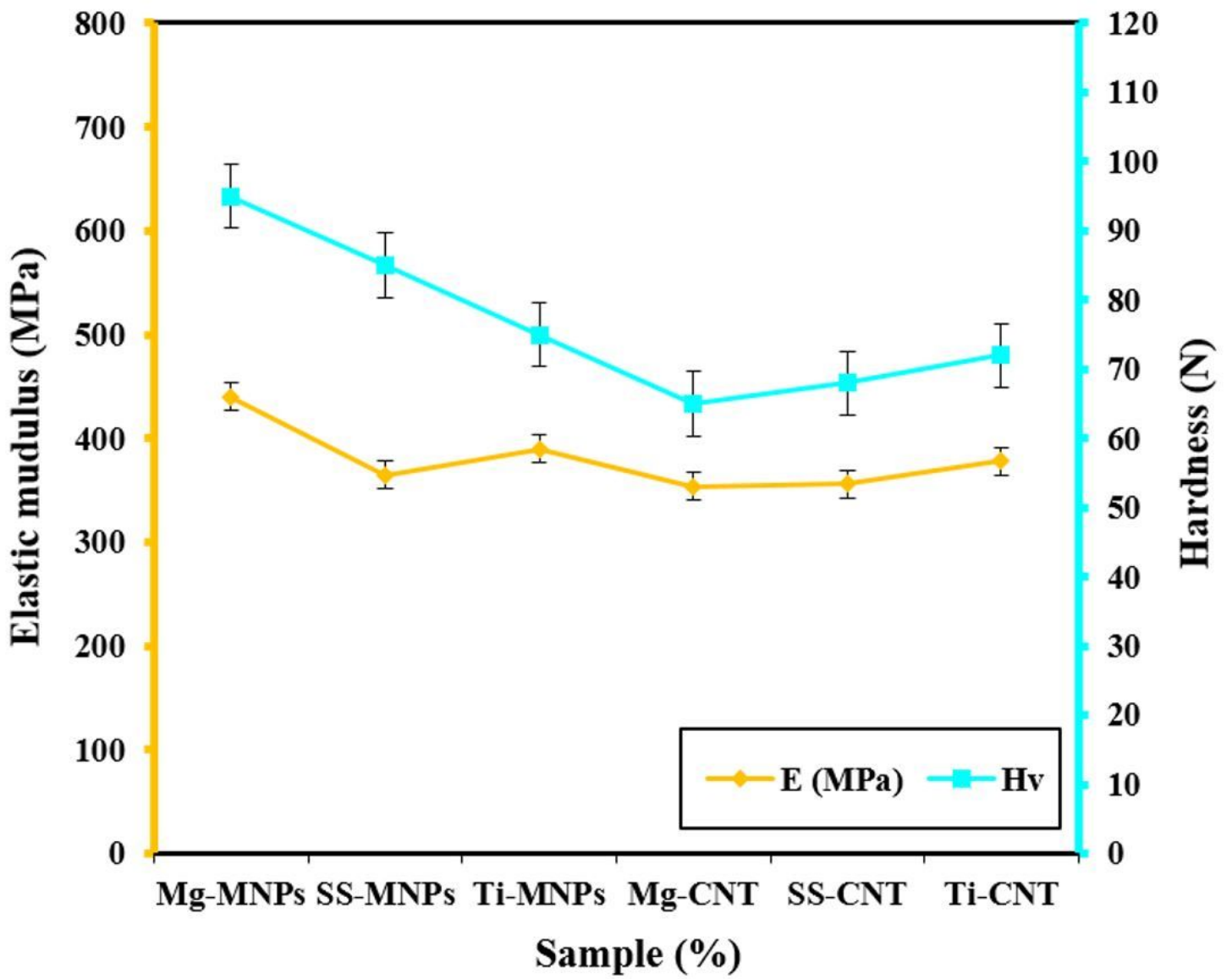


Figure 9

Results of the strength modulus comparison of micro hardness coatings on different alloys by nano-induction device

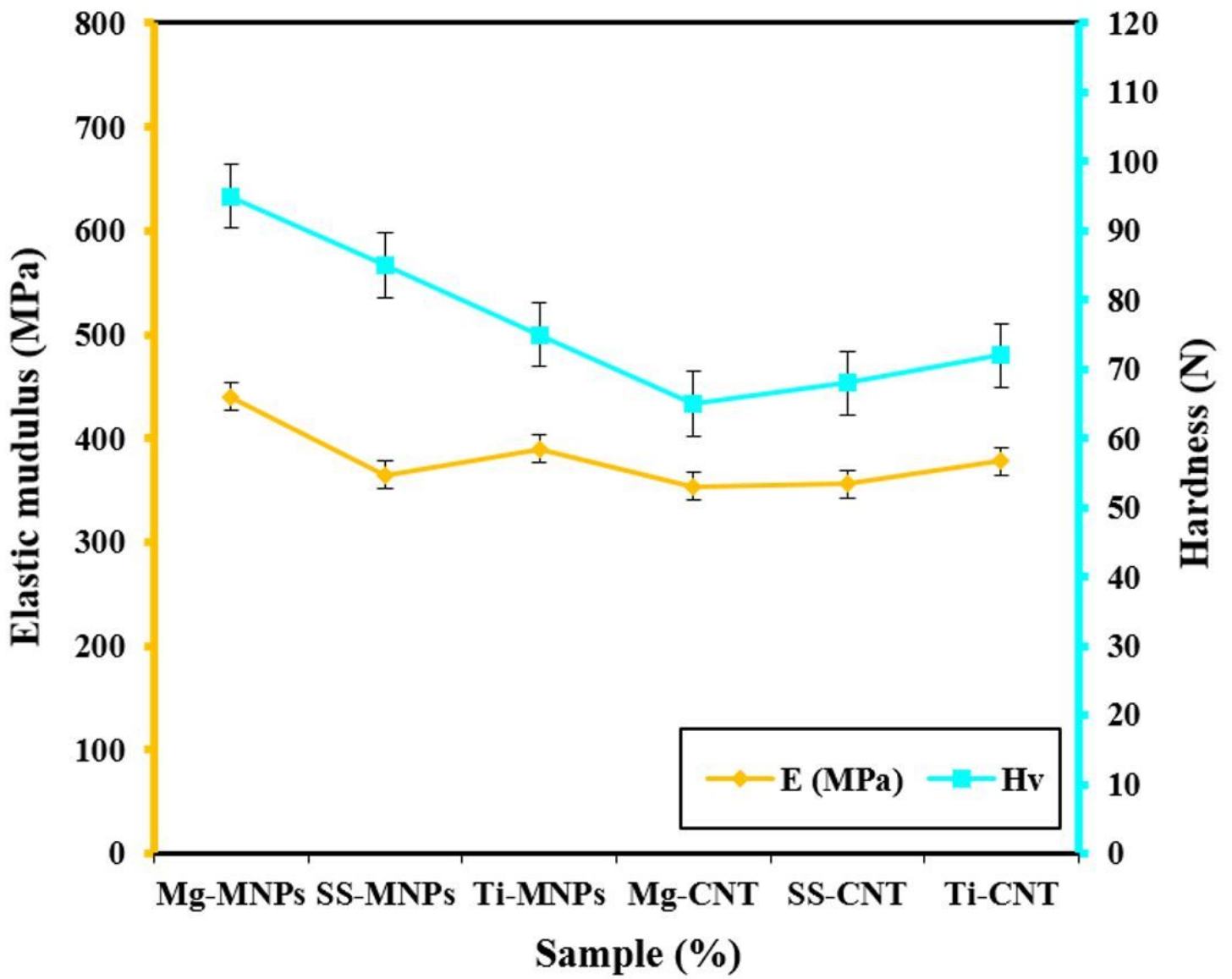
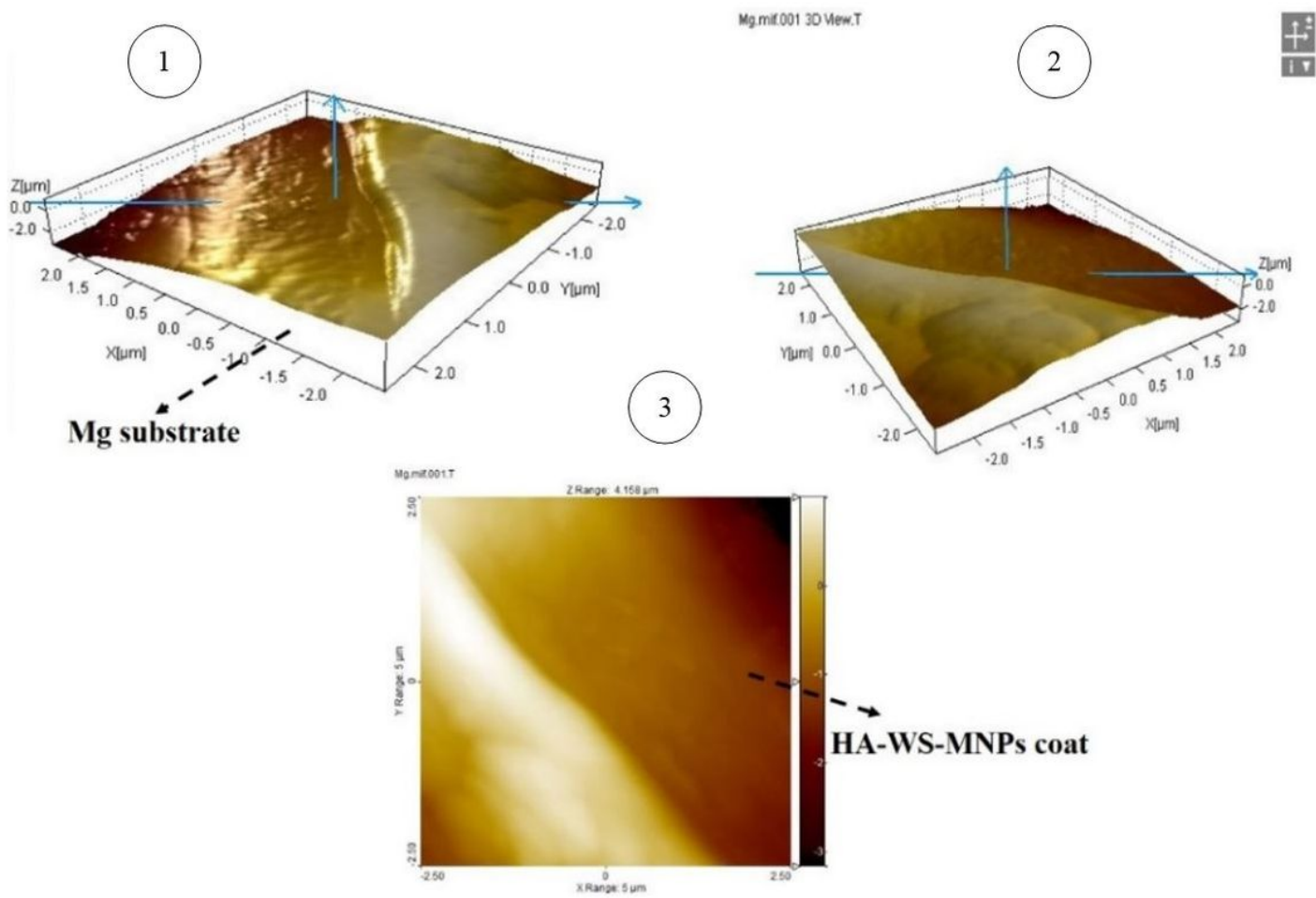


Figure 9

Results of the strength modulus comparison of micro hardness coatings on different alloys by nano-induction device



**Figure 10**

AFM microscope image of the surface of the prosthetic coating coated with hydroxyapatite-wollastonite-magnetic nanoparticle by electrophoretic method on the Mg alloy substrate

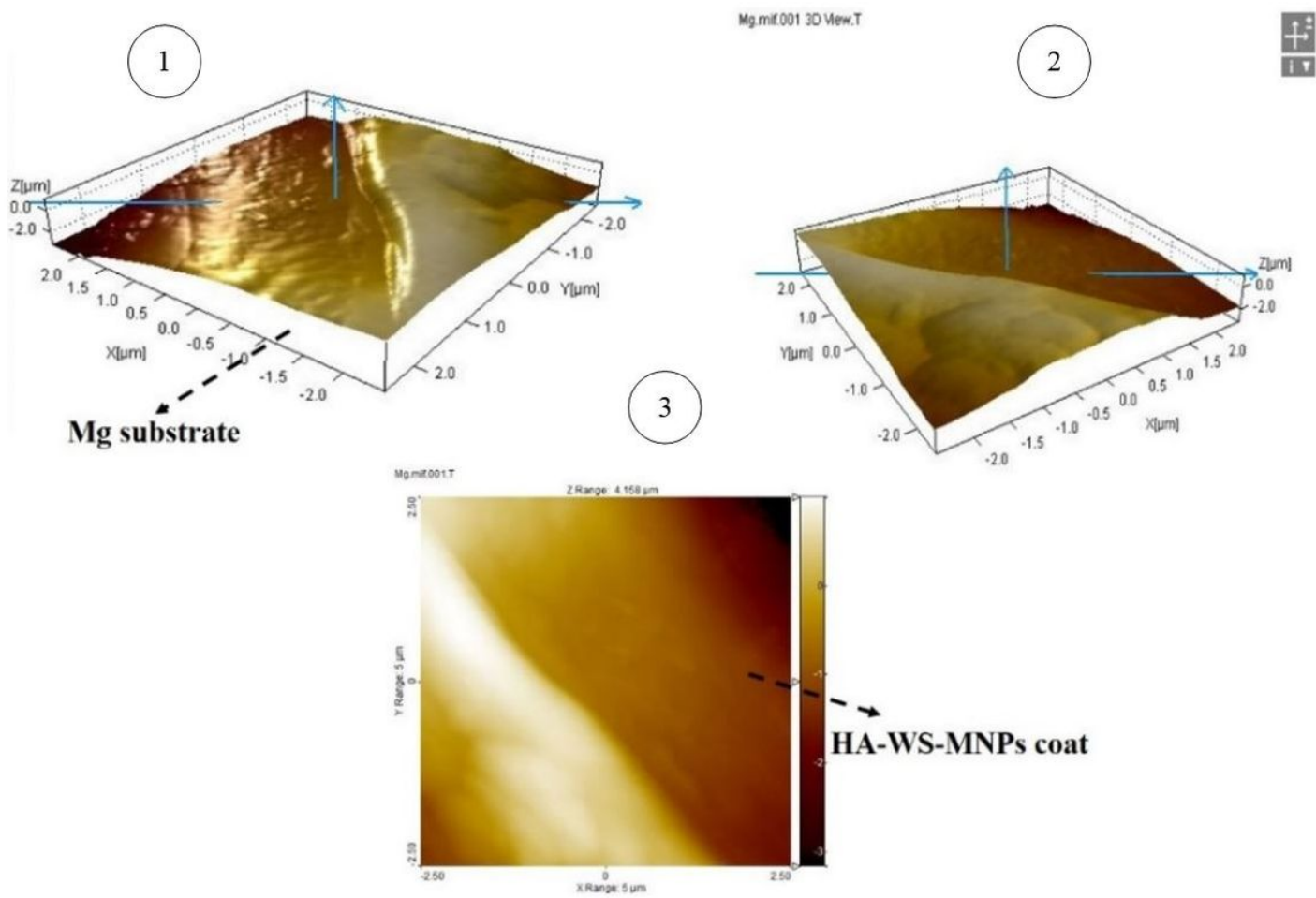


**Figure 10**

AFM microscope image of the surface of the prosthetic coating coated with hydroxyapatite-wollastonite-magnetic nanoparticle by electrophoretic method on the Mg alloy substrate

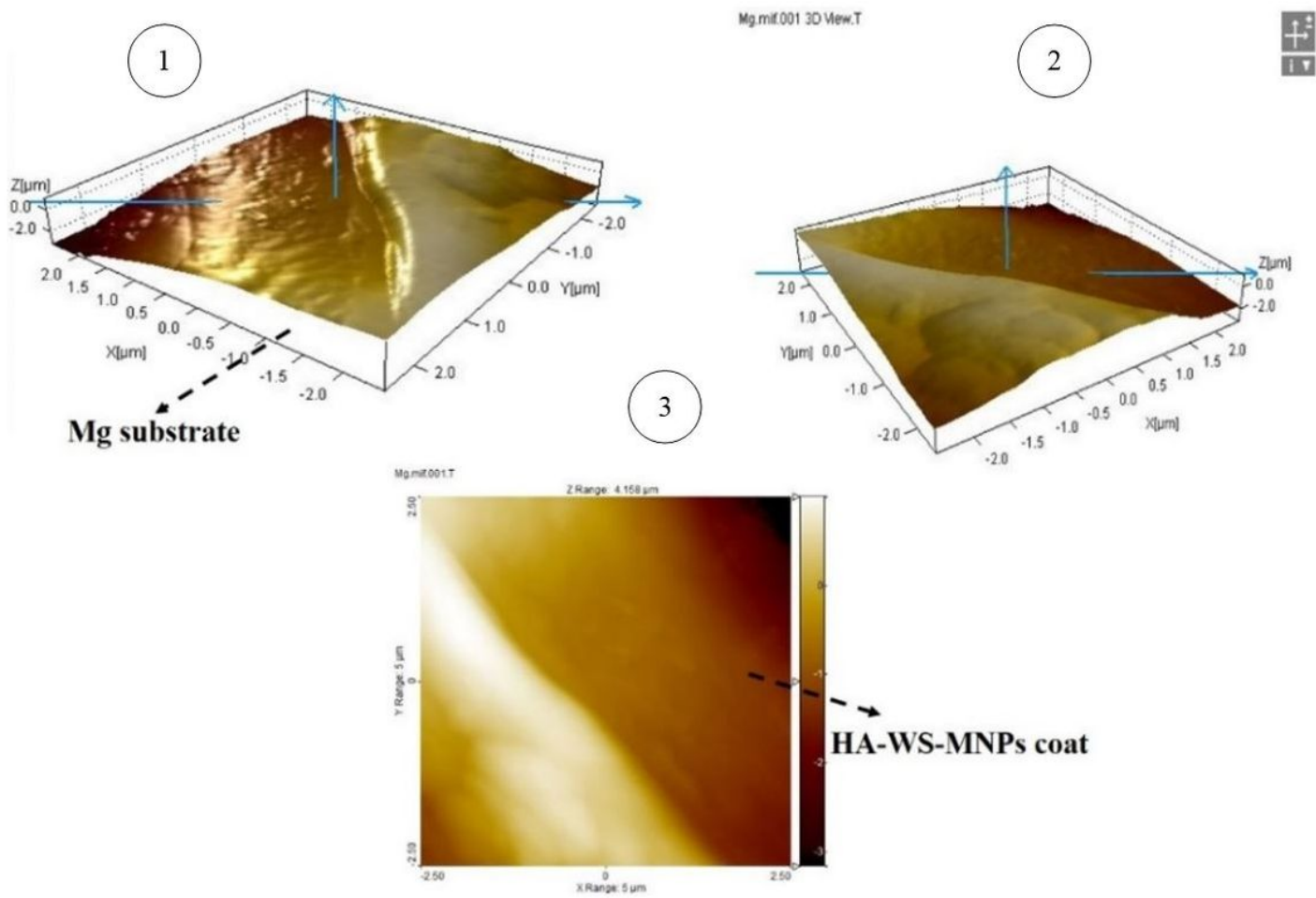


**Figure 10**

AFM microscope image of the surface of the prosthetic coating coated with hydroxyapatite-wollastonite-magnetic nanoparticle by electrophoretic method on the Mg alloy substrate

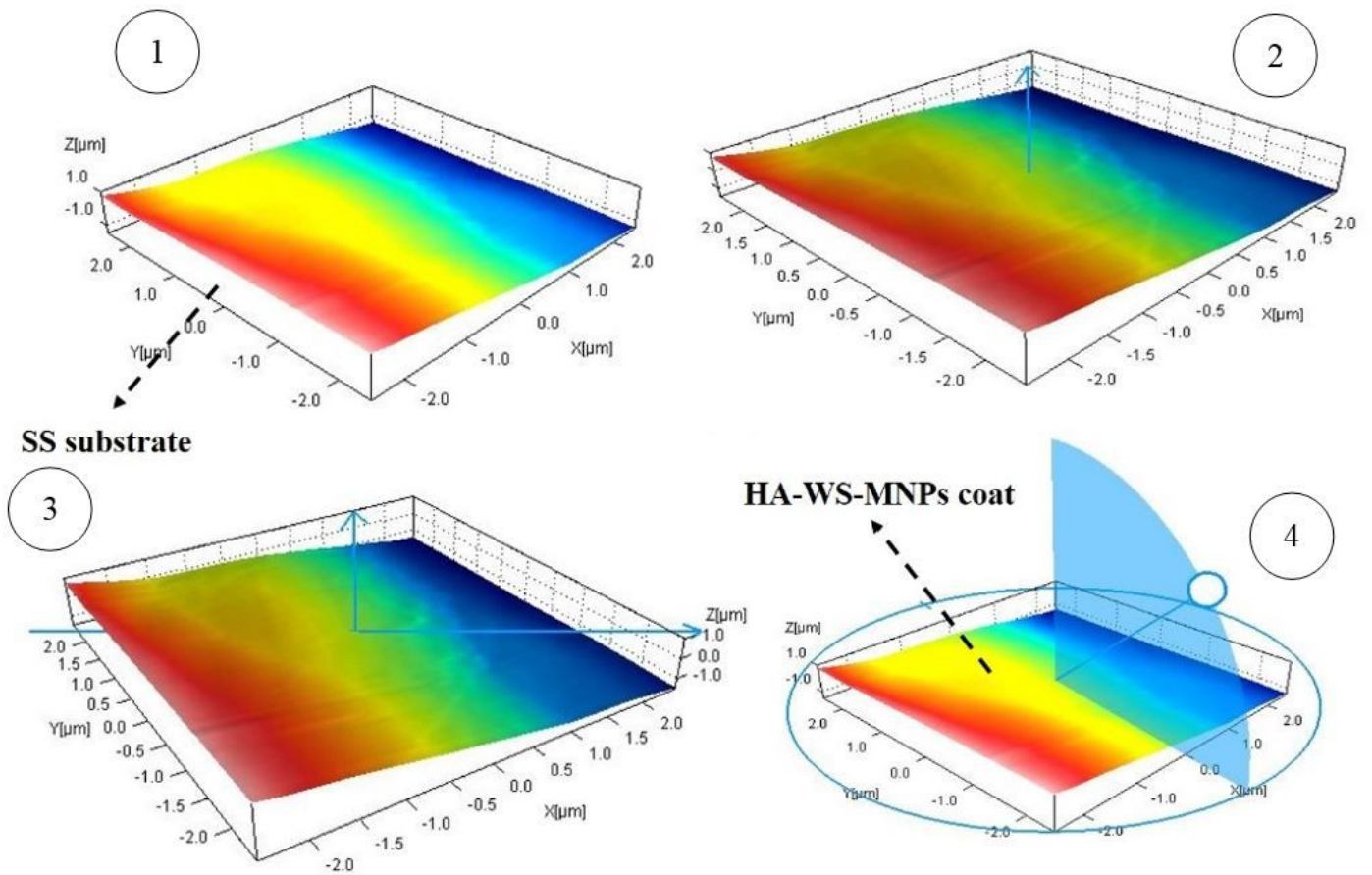


**Figure 11**

3D and confocal AFM microscope image of sample surface coated electrophoretic on stainless steel alloy with hydroxyapatite-wollastonite-magnetic nanoparticle bio-nanocomposite

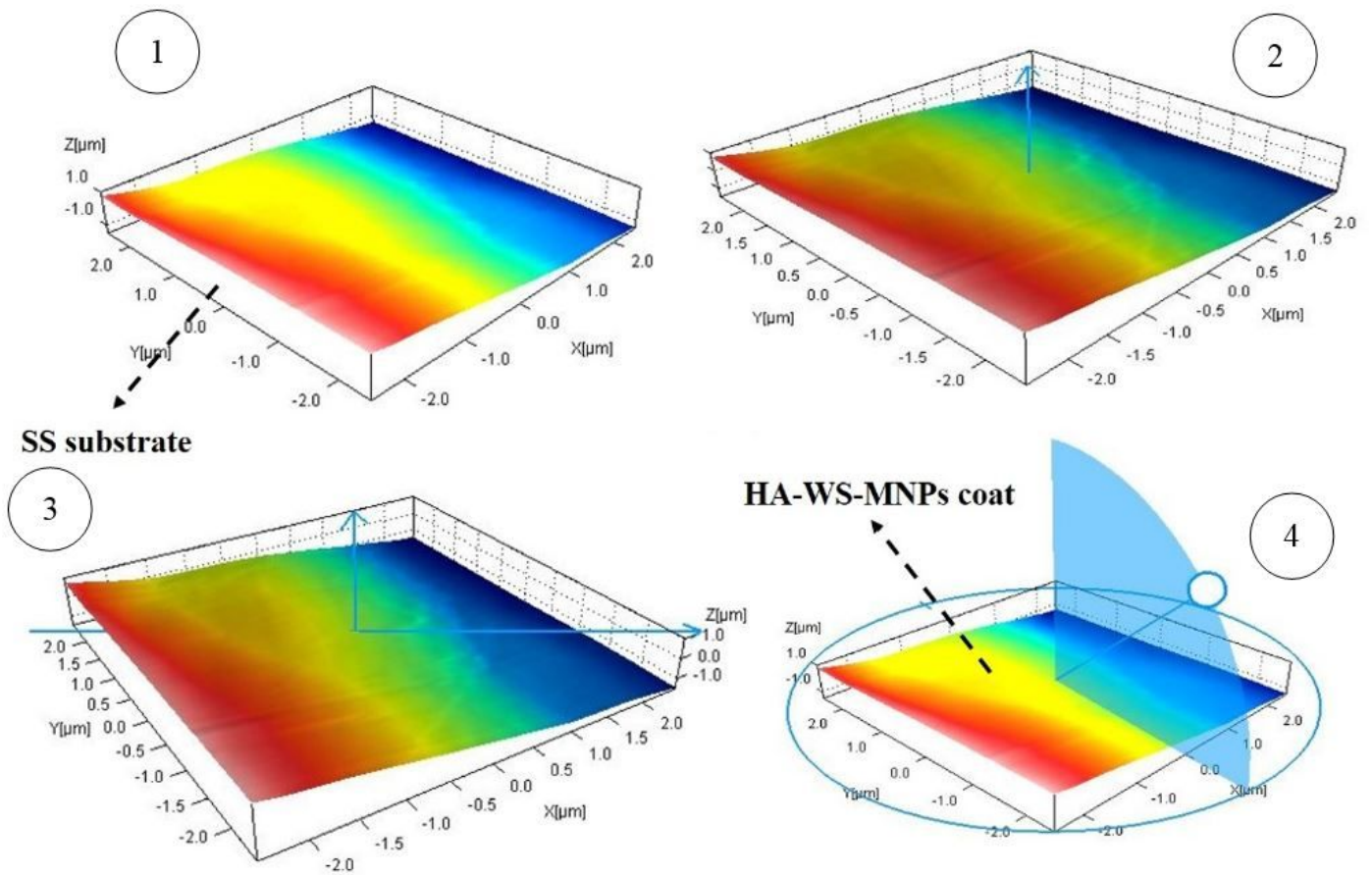


**Figure 11**

3D and confocal AFM microscope image of sample surface coated electrophoretic on stainless steel alloy with hydroxyapatite-wollastonite-magnetic nanoparticle bio-nanocomposite

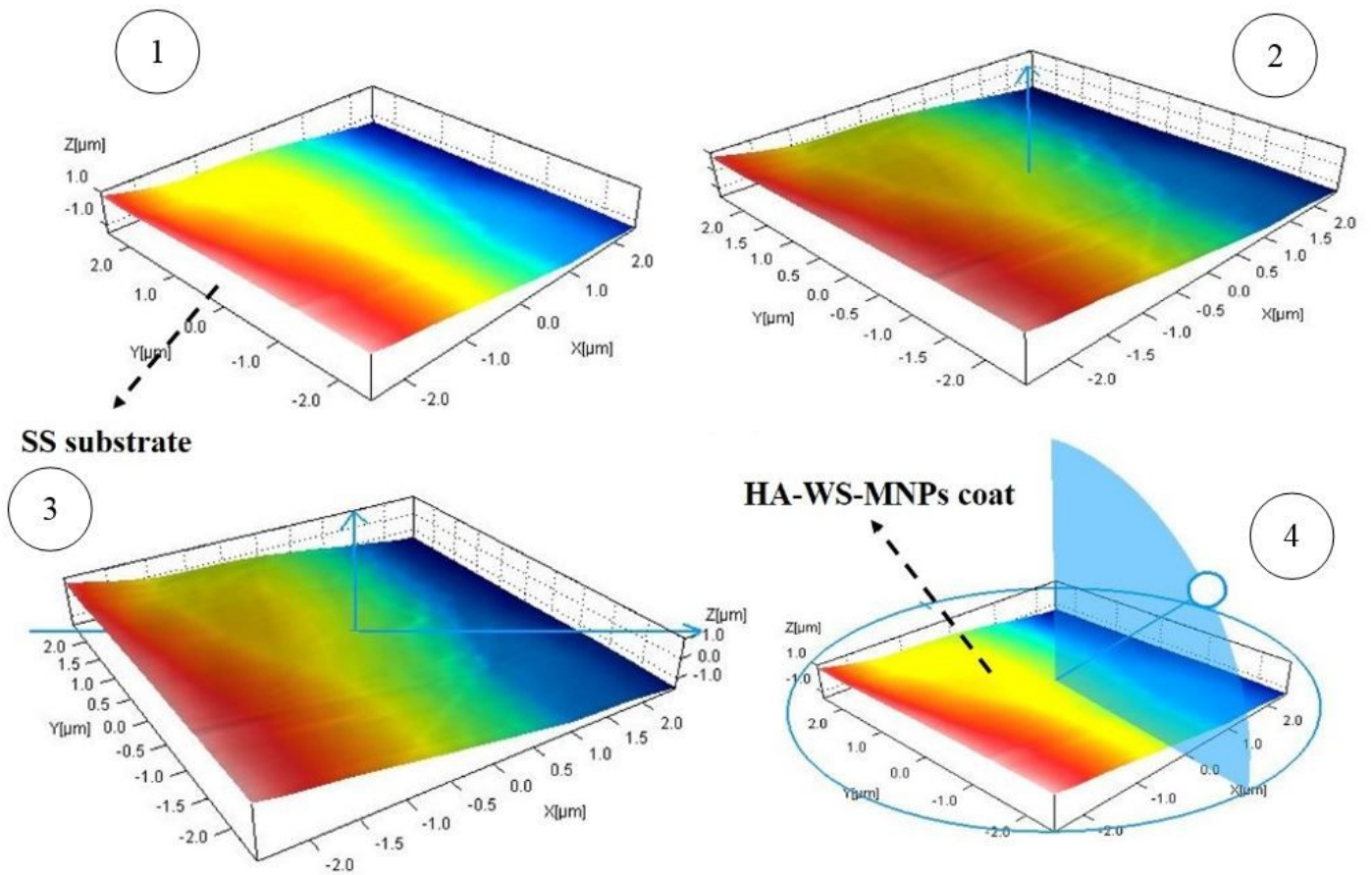


**Figure 11**

3D and confocal AFM microscope image of sample surface coated electrophoretic on stainless steel alloy with hydroxyapatite-wollastonite-magnetic nanoparticle bio-nanocomposite

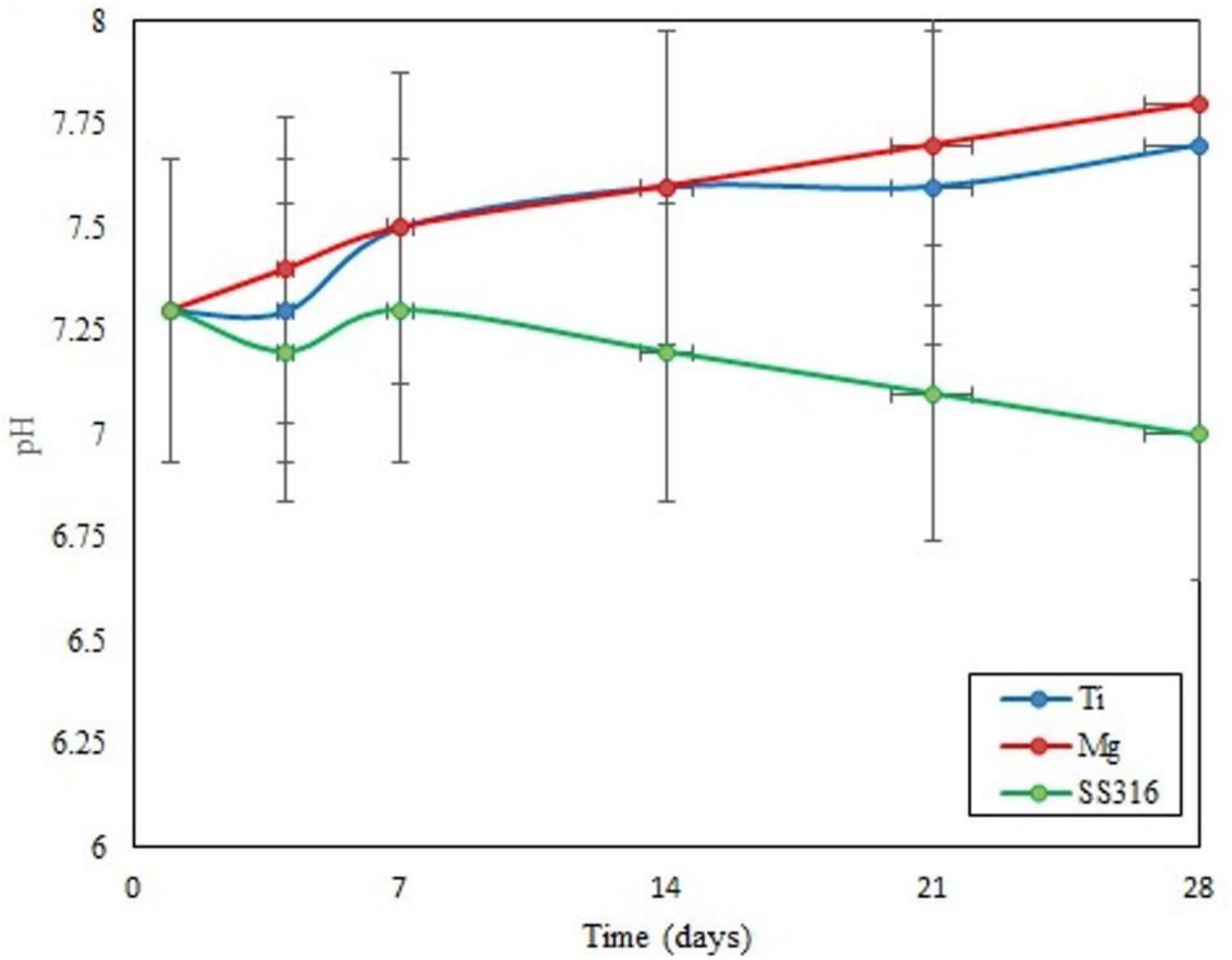


**Figure 12**

Results of the strength modulus comparison of micro hardness coatings on different alloys by nano-induction device

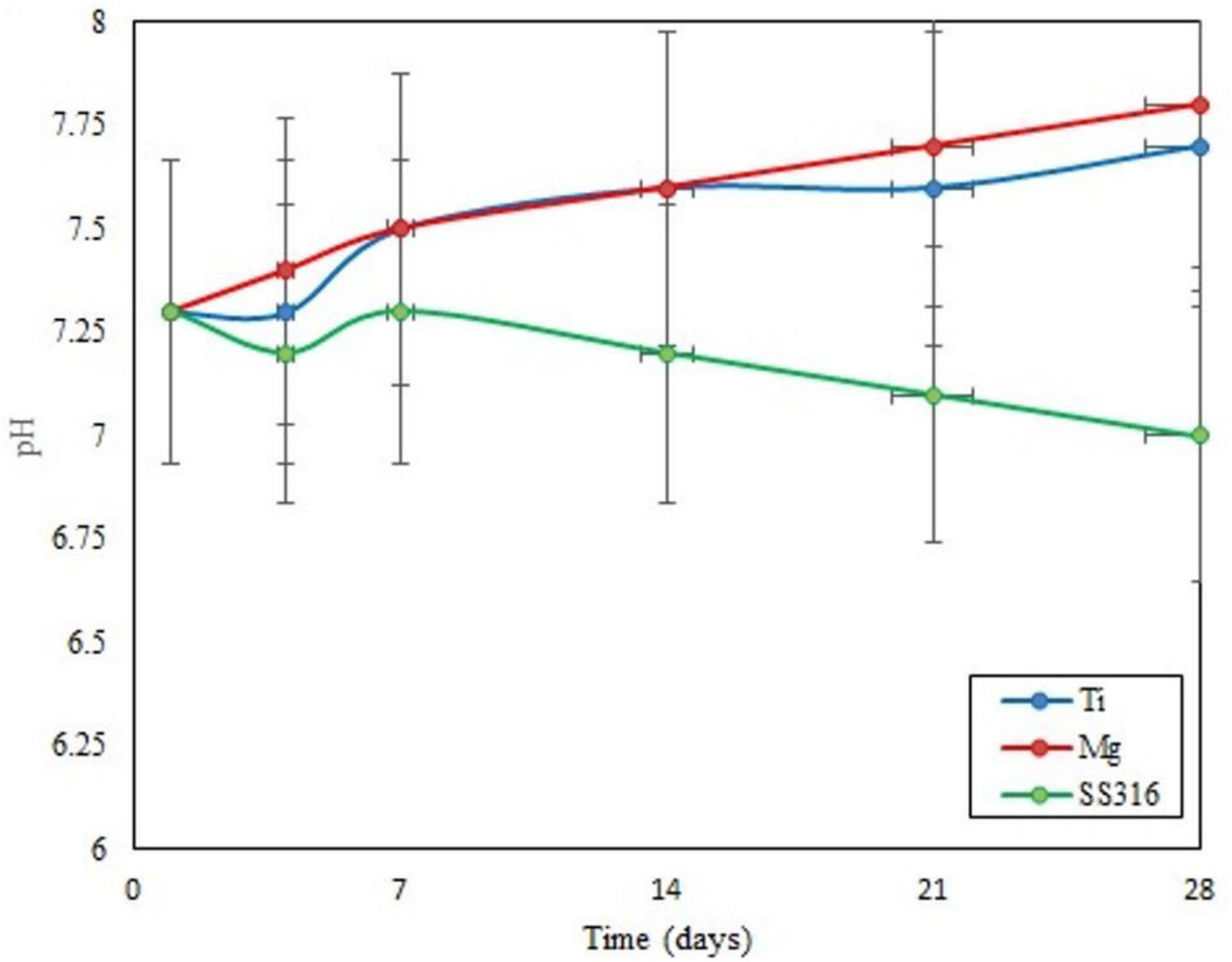


**Figure 12**

Results of the strength modulus comparison of micro hardness coatings on different alloys by nano-induction device

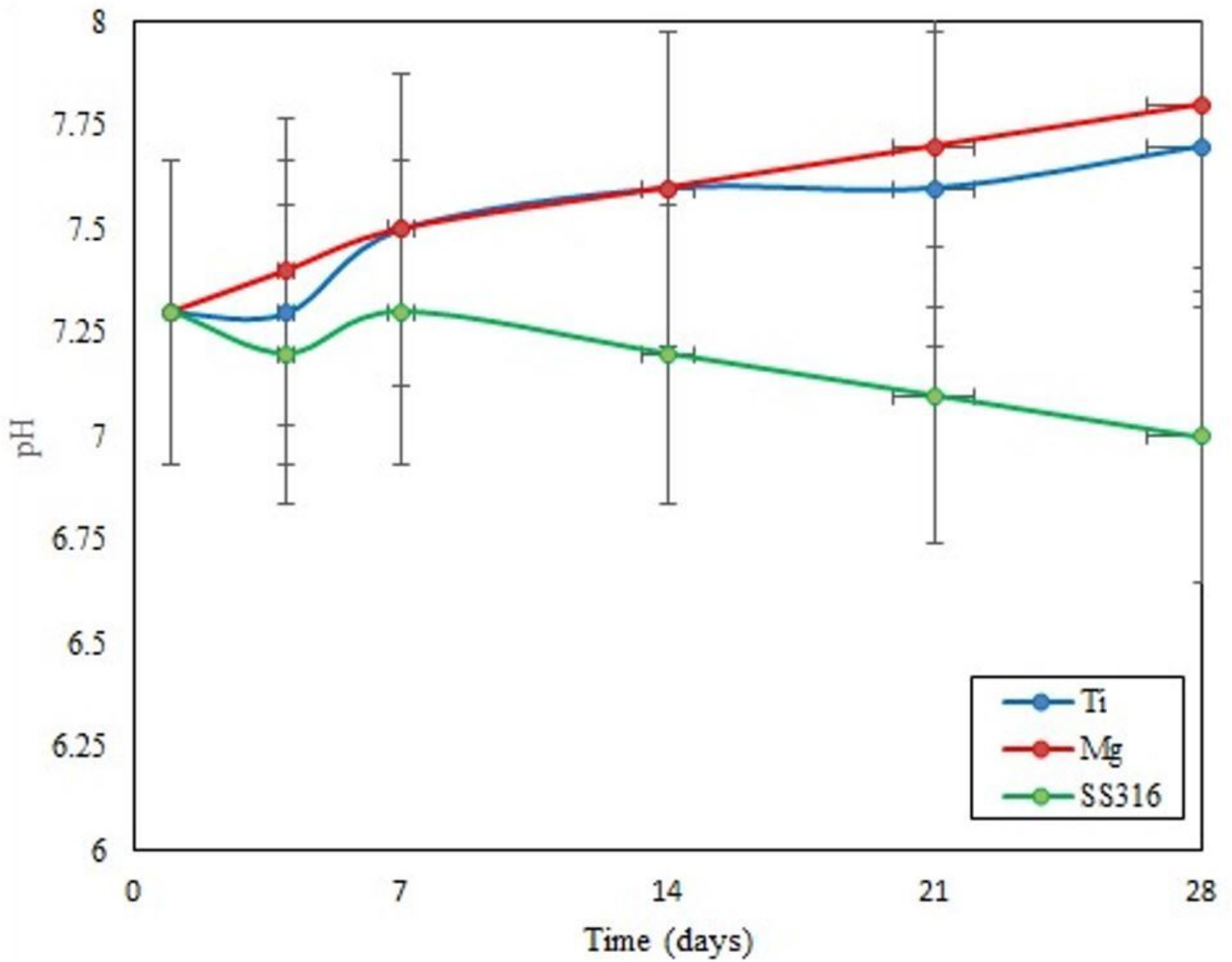


**Figure 12**

Results of the strength modulus comparison of micro hardness coatings on different alloys by nano-induction device

## Supplementary Files

This is a list of supplementary files associated with this preprint. Click to download.

- [GraphicalAbstract.docx](#)
- [GraphicalAbstract.docx](#)
- [GraphicalAbstract.docx](#)